Version of Record: https://www.sciencedirect.com/science/article/pii/S0925838821047472
Manuscript_9ce2d5d527ead66a17d4040428dbf4dc

Surface enhanced performance of $La_{0.6}Sr_{0.4}Co_{0.2}Fe_{0.8}O_{3-\delta}$ cathodes by infiltration Pr-Ni-Mn-O progress

Yongjing Shi[1,2,3], Yeting Wen[2], Kevin Huang[2*], Xiaolei Xiong[2], Jie Wang[2], Meilin Liu[3*], Dong Ding[3], Yu Chen[3], Tong Liu[4]

1. School of Metallurgy and Materials Engineering, Chongqing University of Science and Technology, Chongqing 401331, PR China

2. College of Engineering and Computing, University of South Carolina, Columbia, SC 29208, USA

3. School of Materials Science and Engineering, Georgia Institute of Technology, Atlanta, GA 30332-0245, USA

4. School of Power and Mechanical Engineering, Wuhan University, Wuhan 430072, PR China

Corresponding author: shiyongjing@cqust.edu.cn, Huang46@cec.sc.edu, meilin.liu@mse.gatech.edu

Abstract

The present study reports the enhancement of electrochemical oxygen reduction activity of porous $La_{0.6}Sr_{0.4}Co_{0.2}Fe_{0.8}O_{3-\delta}$ (LSCF) cathodes by coating a thin film of Pr-Ni-Mn oxide (PNM5) using a multi-step infiltration process. XRD examination reveals that PNM5 mainly contains a multiphase mixture of Pr_6O_{11}, $PrNiO_3$, MnO and NiO. SEM morphology shows a thin PNM5 film and small particles are formed on the surface of LSCF backbone particles. Impedance spectrum analysis indicates that PNM5 infiltrated LSCF exhibits dramatically reduced polarization resistance (R_p), reaching R_p of 0.244 $\Omega\,cm^2$ at 973K, which is one-half of the baseline LSCF cathode. The activation energy of LSCF cathodes infiltrated with PNM5 is 1.45 eV, slightly lower than the baseline LSCF cathode (1.77 eV). Distribution of relaxation time (DRT) function analysis shows PNM5 infiltration layer significantly promotes the oxygen reduction reaction (ORR) of cathode surface. With the increase in firing temperature, the total resistance increases

© 2022 published by Elsevier. This manuscript is made available under the Elsevier user license
https://www.elsevier.com/open-access/userlicense/1.0/

and R_p changes from ion transport to oxygen reduction reaction. Degradation rate of the PNM5-infiltrated LSCF is also lower, 0.02168% vs 0.07093% for the baseline LSCF over a 200-h period. A single cell testing indicated that the peak power density of the PNM5-infiltrated cell was increased by 140.66%. Overall, PNM5 could be a potential catalyst for boosting the performance of a commercial LSCF cathode for solid oxide fuel cells (SOFC).

Keywords: solid oxide fuel cell, infiltration, distribution of relaxation, time stability

Ⅰ. Introduction

The concerns over global climate change and dwindling of the available fossil fuel resources call for development of new efficient and clean energy conversion technology. Fuel cells are a type of such clean energy technologies [1-3]. Among all types of fuel cells, SOFCs stand out to be an unparalleled hydrocarbon-to-electricity energy converter [4, 5]. However, to commercialize the SOFC technology, the operating temperature of SOFC must be reduced from the current 973-1073K to below 973K, at which both cost reduction and durability enhancement, the two major challenges facing SOFC commercialization, can be realized. To achieve reduced operating temperature of SOFCs, cathode development needs to lead the way since cathode polarization dominates the overall performance of a RTSOFC [6-9].

There are two ways to reduce R_p: discovering new materials and surface modification of existing cathode materials [10, 11]. The latter approach is practically attractive because it brings the minimum change to manufacturing processes of SOFC industry. The past few decades, LSCF perovskite is a state of the art mixed ionic–electronic conducting cathode materials for IT-SOFCs[12]. It is reported that LSCF perovskite has a high ionic conductivity and electrical conductivity with 10^2 $S \cdot cm^{-1}$ at 1073K， as well high oxygen diffusion properties, but the overall oxygen reaction $O_{2,gas}+4e^- \rightarrow 2O^{2-}$ at LSCF cathodes occurs is limited by surface or interfacial processes[13, 14]. LSCF is the R3c space group with near-cubic perovskite-type phase of the ABO_3 structure with trivalent transition metal ions in the B site and a trivalent

rare earth in the A site, but its structure and electric conductivity depends on the atomic ratio of La and Sr at the A site and the atomic ratio of Co and Fe at the B site[15, 16]. Fan et al have reported that the oxygen ion conductivity of $La_{0.54}Sr_{0.44}Co_{0.2}Fe_{0.8}O_{3-\delta}$ is nearly five times higher than that of $La_{0.6}Sr_{0.4}Co_{0.2}Fe_{0.8}O_{3-\delta}$[17]. As the thickness of the cathode increased, more active sites for the electrochemical reaction are added and the R_p decreased[18]. Jang et al shows the structure, porosity and particle size of LSCF coating is mainly dependent on the heat treatment temperature[19]. Recently, a novel anion doping strategy have emerged in the study of new materials, such as the doped perovskite $La_{0.6}Sr_{0.4}Co_{0.2}Fe_{0.8}O_{2.95-\delta}F_{0.05}$[20-22]. It is reported in the literature that surface modification of onto LSCF cathode significantly reduced the R_p, the encouraging results open a promising strategy to develop cathode materials for H–SOFCs at low temperature[23, 24]. Therefore, surface modifications of the state-of-the-art cathode LSCF by independent catalysts to improve the intermediate-temperature performance has drawn significant interest in recent years [25-27]. The surface ORR on LSCF particles or the exchange reaction of oxygen between gas phase and solid is considered as a major governing factor that determines the operating temperature of SOFC, i.e., high oxygen vacancy concentration and vacancy mobility are key factors for the surface oxygen exchange rate[28-30].

Recently, the Pr-Ni-O system has attracted widespread attention as the cathode of a fuel cell due to its ion transport characteristics similar to LSCF, it mainly includes A_2MO_4 and AMO_3 perovskite oxides, in which the K_2NiF_4-structured A_2MO_4 comprise of alternate layers of AMO_3 perovskite and AO rock-salt sublayers[31-33]. Some early studies indicated that A_2MO_4 oxides possess good oxygen permeability and comparable oxygen surface exchange rate [34]. The praseodymium nickelate system $Pr_2NiO_{4-\delta}$ is of particular interest because of the mixed valence on Pr and high oxygen exchange coefficient [35]. However, this material is thermally unstable, decomposing into Pr_6O_{11} and $Pr_4Ni_3O_{10}$ after exposing at 973K for 24 h [36]. Doping on A-site and/or B-site of A_2MO_4 such as $Pr_{2-x}Sr_xNiO_{4+\delta}$ (x =0.3–1.0),

$Pr_2Ni_{0.71}Cu_{0.24}Ga_{0.05}O_4$, $Pr_{0.7}Sr_{0.3}Fe_{1-x}Cu_xO_{3-\delta}$ and $(Pr_{0.9}La_{0.1})_{2-x}(Ni_{0.74}Cu_{0.21}Al_{0.05})O_{4+\delta}$ (with x=0, 0.05, and 0.1) as cathodes [37-40], have been shown with improved mixed conductivity and stability. In the present study, we report the use of Pr-Ni-Mn Oxide as a catalyst to improve the perofrmance of a porous LSCF cathode; the nano catalyst layer is incorporated into the LSCF porous scaffold as nanoparticles by a multi-step infiltration approach.

Ⅱ. Experimental Procedure

2.1 Synthesis of Pr-Ni-Mn-O and LSCF

A series of Pr-Ni-Mn oxide powder samples with different metal atom ratio including PN (Pr: Ni-2:1), PNM2.5 (Pr:Ni:Mn-2:0.975:0.025), PNM5 (Pr:Ni:Mn-2:0.95:0.05) and PNM10 (Pr:Ni:Mn-2:0.9:0.1) powders were synthesized by a nitrate citric acid method. The stoichiometric amount of starting $Pr(NO_3)_3{\cdot}6H_2O$, $Ni(NO_3)_2{\cdot}6H_2O$ and $Mn(NO_3)_3{\cdot}4H_2O$ (Alfa Aesar, 99.98wt%) were first dissolved into DI water solution (20% Ethanol). The complexation agent of citric acid and Editic acid (EDTA) was then added at a molar ratio of citric acid/EDTA/metal at 1.5:2:1. Subsequently, in order to facilitate the complexing of metal ions, the pH of the solution is adjusted to 7-8 by the addition of aqueous ammonia. The precursor solution was complexed about 3 h at 373K, and the resultant gel was fired at 873K and 1073 K for 3 h each to obtain fine powders. The LSCF powder used to measure electrical conductivity is synthesized by a similar combustion method. The materials used are $La(NO_3)_2{\cdot}6H_2O$, $Sr(NO_3)_2{\cdot}4H_2O$, $Co(NO_3)_2{\cdot}6H_2O$ and $Fe(NO_3)_2{\cdot}9H_2O$ according to the atomic ratio of 6-4-2-8. The firing temperature of the powder is 1473K.

2.2 Fabrication of symmetrical cells

Symmetrical cells were fabricated using gadolinia-doped ceria (GDC) as electrolyte and porous LSCF skeleton infiltrated with PNM5 nanoscale particles as electrodes. The GDC electrolyte pellets were prepared by isostatic pressing and subsequently firing GDC powders at 1673K for 5 h. The electrolyte

pellets fired were about 16.36 mm in diameter and 0.5 mm in thickness. A commercial LSCF cathode ink purchased from Fuel Cell Materials was screen printed onto GDC surfaces three times, followed by firing at 1353K for 2 h to form a well bonded porous LSCF cathode skeleton.

2.3 Infiltration of catalysts

In order to show the special catalyst behavior of PNM5, at first the infiltration solution of PN, PNM2.5, PNM5 and PNM10 were prepared by mixing stoichiometric amount of $Pr(NO_3)_3 \cdot 6H_2O$, $Ni(NO_3)_2 \cdot 6H_2O$ and $Mn(NO_3)_3 \cdot 4H_2O$ (Alfa Aesar, 99.98wt%). The above nitrates were first dissolved into ethanol to improve wettability of nitrite solutions on porous LSCF backbones, followed by adding complexation agent of citric acid at a molar ratio of citric acid/metal of 1:1. The nitrate concentration was 0.15M, 0.2M and 0.25M. The above solutions were then added into the porous LSCF skeleton drop by drop, after which, the symmetrical cells were gradually fired for one hour at 973, 1023, 1073, 1123 and 1173K, respectively. The actual loading of infiltrated species was controlled by Scilogex variable volume Pipettor.

2.4 Cell performance testing

Electrolyte-supported cells, NiO (65%) + GDC (35%)/GDC/LSCF and NiO (65%) + GDC (35%) /GDC/LSCF infiltrated with PNM5, were fabricated using gadolinia-doped ceria (GDC) as electrolyte and porous LSCF skeleton infiltrated with PN, PNM2.5, PNM5 and PNM10 nanoscale particles as electrodes. NiO (65%) + GDC (35%) is anode and NiO is used for fuel catalysis. The GDC electrolyte pellets were prepared by isostatic pressing and subsequently sintering GDC pellets at 1673K for 5 h. The sintered electrolyte pellets were about 16.36 mm in diameter and 0.5 mm in thickness. After polishing, the anode pastes, NiO (65%) +GDC (35%) was printed on a side of electrolytes by screen print method, followed by firing at 1673K for 4h. A commercial LSCF cathode ink purchased from Fuel Cell Materials was screen printed onto GDC surfaces three times, followed by firing at 1353K for 2 h to form a well bonded porous LSCF cathode skeleton. The LSCF electrode has a 15~20 μm thickness and 1.33 cm^2 effective area.

A single SOFC was constructed by an alumina tube and was sealed by glass powder of high temperature. Silver mesh and wires used as the current collector were bonded on the anode and cathode on both sides of single cell by silver paste and fired at 873K for 2 h. The glass powder was fired at 1073K for 15 minutes before flowing the Hydrogen gas. After the in-situ reduction of the NiO anode in H_2 for several hours, the performances of the cell were measured at various temperatures from 750 to 650°C. Hydrogen passed over the anode at a flow rate of 50 mL/min. The AC impedance spectrum was measured at an excitation potential of 10 mV and a frequency range of 1 MHz to 0.01 Hz under open-circuit conditions using a 1255/1287 Solartron Electrochemical System.

2.5 Characterization

The element composition and chemical composition of powder samples was detected by Inductively Coupled Plasma Optical Emission Spectrometer (ICPOES, Agilent 720ES) and PANalytical's Zetium X-ray fluorescence spectrometry (XRF). The phase structure of these samples was examined by powder X-ray diffraction (PXRD) using an X-ray diffractometer (D/max-A, Rigaku) with graphite-monochromatized CuKa radiation (λ= 1.5418 Å). The XRD scan was performed at a rate of 5º min^{-1} from 20º to 80º. The XRD patterns were further analyzed with the JADE software to identify the phase structure and composition. The electric conductivity of samples was measured by high temperature comprehensive physical property measurement system. The electrical conductivity was measured by a four-probe method applying direct current (DC) in air in a cooling mode from 1073 to 473K. The step of measurements was 50K with an exposure time of 0.5 h and a heating/cooling rate of 2K/min. The cross-sectional view of microstructure of the cells was captured by a field-emission scanning electron microscopy (FESEM, Zeiss Ultra). The microstructure and composition of LSCF cathode with infiltration PNM5 was captured by field emission transmission electron microscope.

2.6 Data fitting

The AC impedance spectrum is fitted by ZView and ZSimpWin software. The fitted equivalent circuit and Nyquist plot are used to explain the evolution of the ORR process and ion transport. The fitting error is less than 10%. DRT is also an important method of analyzing AC impedance spectrum and revealing oxygen transport resistivity, it is an effective supplement to the equivalent circuit used to explained oxygen transport progress [41, 42]. DRT analysis identifies the characteristic time constant distribution of impedance data, and the impedance spectrum is represented as an infinite sum of series–connected parallel RC–circuits each one having the resistivity $R_p\gamma(\tau)d\tau$. The fitting experimental data at various frequencies with a model used the following expression:

$$Z(\omega) = R_\infty + R_p \int_0^\infty \frac{\gamma(\tau)d\tau}{1 + i\omega\tau}$$

Here, R_∞ represents the cell ohmic resistance; The function γ(τ) is the distribution of relaxation times for the cell impedance spectrum. This calculation process is realized by running the DRT program on the MATLAB platform, and this peak fitting is a deconvolution calculation process. Method of discretization is Gaussian; Radial Basis Functions Discretization shape control is the full width at half maximum (FWHM) coefficient with the magnitude of 0.5 as default.

Ⅲ. Results and discussions

3.1 Microstructure

The element mass and compound composition of powder samples is shown in Table 1 by ICPOES and XRF, the results show that the oxide in these powder samples are MnO, NiO and Pr_6O_{11}. XRD patterns of PN, PNM2.5, PNM5, PNM10 are shown in Fig.1(a). The pure PN shows a mixture phase consisting of Pr_6O_{11} (PDF# 421121) and NiO (PDF# 221189). Some research revealed the K_2NiO_4-type structure phase containing Pr was prepared in air at above 1573K by a conventional solid-state reaction route [43, 44]. So, the K_2NiO_4-type structure phase containing Pr could be not prepared at 1073K. After 2.5% Mn was

substituted into Ni, it is found that Pr_6O_{11}, NiO and MnO (PDF# 750257) emerge as impurity phases. But the diffraction peaks of $PrNiO_3$ (PDF# 801359) phase could be also seen in powder samples. P. Lacorre et al prepared pure $PrNiO_3$ samples at 1273K for several days under 150-200 bars of oxygen with several intermediate regrinding and repressing[45]. VaibhavVibhu et al reported that $PrNiO_{3-\delta}$ phase can be synthesized at firing temperature of 1123K for 48 h under oxygen flow conditions [46]. But this $PrNiO_{3-\delta}$ phase cannot be synthesized under 1073K conditions, as shown in the Fig. S1. Similarly, the $PrNiO_{3-\delta}$ phase cannot be formed in the stoichiometric $PrNiO_{4-\delta}$ system. So, the formation of $PrNiO_3$ phase is related to the addition of Mn element in Pr-Ni-Mn-O system. Pr_6O_{ll} originates from mother phase PrO_2 with the fluorite structure, but they all belong to the Fm3m space group, and the thermal analysis indicates PrO_2 and P_6O_{11} can coexist[47, 48]. As a result, PNM2.5, PNM5 and PNM10 samples mainly contains Pr_6O_{11}, NiO and MnO phase. Moreover, the XRD patterns of LSCF and LSCF infiltrated with PNM5 is shown in Fig.1(b), which indicate that the XRD results are the same before and after infiltration, the diffraction intensity of LSCF drowned that of the PNM5 infiltrated layer because there are very thin infiltration layers.

3.2 Morphology characteristics

Cross-sectional views of LSCF cathode infiltrate with PNM5 are shown in Fig.2. From these typical SEM images, it is evident that LSCF skeleton surface is covered with a uniform coating of PNM5 thin film; some nanoscale particles among the skeleton are also observed, as shown in the blue oval circle in Fig. 2 (d) and Fig. 2 (f), similar to those reported in the literature[24, 49]. To further reveal the microstructure and morphology of PNM5 on LSCF, TEM picture and STEM mapping picture of LSCF cathode infiltrate with PNM5 was obtained, as given in Fig.3. It reveals that the PNM5 on LSCF skeleton is a thin film with a thickness of 40-70nm, as shown by the yellow pointed head. TEM Mapping detection shows that the Ni concentration distribution is obviously circular around the particles, which is consistent with the structure shown in TEM pictures. However, the Ni concentration distribution is not circular, indicating infiltration

layer on the whole surface of cathode particles is inhomogeneous. Due to the low content, the energy spectrum of Mn is not captured. After the stability measurement at 973K for 200 h, particle coarsening of infiltration PNM5 on surface of LSCF is not observed, indicating that PNM5 as a surface catalysis is stable in microstructure.

3.3 Electric conductivity

Shown in Fig.4 is the temperature dependence of the Pr-Ni-Mn oxide in total electrical conductivity (σ). These samples must be pressed into strips before being detected. It demonstrates a different temperature dependent characteristic, total σ value of PN sample is higher than other samples and PNM10 sample has the lowest σ value. It almost coincides for σ value curve of PNM5 and PNM2.5 samples. The maximum σ value PNM5 sample is 95.48 $S \cdot cm^{-1}$ in 773K. It is reported the maximum σ value of LSCF is close to 332 $S \cdot cm^{-1}$ at a firing temperature of 823K, and σ value decrease with the firing temperature increases [15]. The dependence of σ value on temperature mainly depends on the change of oxygen vacancy. LSCF and these oxide components in Pr-Ni-Mn-O systems (PNM5, PNM2.5 and PNM10) including Pr_6O_{11}, NiO and MnO are all p-type semiconductors. σ value increases with increase in temperature is a semiconductor behavior, but the decrease at high temperatures is mainly metal-like conducting behavior due to the decrease of oxygen vacancy concentration. Compared with these oxides in Pr-Ni-Mn-O system, σ value of PNM5 has been significantly improved [50-52].

3.4 The effect of surface modification on polarization resistance

Shown in Fig.5(a) is impedance spectrum of LSCF and LSCF infiltrated with PN, PNM2.5, PNM5, PNM10 from symmetric cell under open circuit conditions at temperature of 1023K. Each spectrum was collected after the cell reached a steady state. To clearly show the difference in the electrode surface polarization behavior, all R_∞ value was subtracted out. The results show that there is a reduction in R_p value of the baseline LSCF cathode by PNM5 infiltration, but other infiltrations with PN, PNM2.5 and

PNM10 increased polarization behavior instead. The LSCF half-cell infiltrated with PNM5 exhibited a R_p value of about 0.165 Ω cm^2 at 1023K, which shows a minimum R_p value in comparison with blank LSCF, PN, PNM2.5 and PNM10. To understand why PNM5 enhances the electrochemical activity, the impedance spectra of LSCF cathode infiltrated with different compositions possibly presenting in PNM5 were further measured and shown in Fig.5(b). The stoichiometric $PrNiO_3$ clearly decrease the O_2 reduction activity, whereas only Pr_6O_{11} increases electrochemical activity. The reason for this phenomenon is that the stoichiometric $PrNiO_3$ is a mixed phase composed of Pr_6O_{11} and NiO, while the conductivity of NiO is lower than that of Pr_6O_{11}. In the PNM5 system, the Pr_6O_{11}, PrO_2 and $PrNiO_3$ phases all have higher conductivity, so LSCF cathode infiltrated with PNM5 has a higher ORR activity than the stoichiometric $PrNiO_3$. Moreover, the effect of solution concentration for infiltrating PNM5 on the area specific R_p value of the resultant cathode is measured, as shown in Fig.5(c). The results show that half-cell infiltrated with PNM5 of 0.25M emerge a R_p value of 0.244Ω cm^2 at 973K, so the best concertation resulting in the lowest R_p value is 0.25M. It implies that different infiltration concentration brings about the difference in microstructure of the overall cell cathode.

To further reveal the oxygen ion transport mechanism, DRT analyzing method is used to fit the AC impedance spectrum, and the obtained results are shown in Figure 6. ORR and oxygen ion transport in the mixed ionic and electronic cathode conductors can be divided into several elemental steps: (1) adsorption and desorption of oxygen on the surface of cathode particles; (2) ORR progress in gas-solid phase interface and three-phase boundary (TPB); (3) oxygen ion transport in cathode; (4) oxygen ion transport in interface between cathode and electrolyte; (5) oxygen ion transport in electrolyte; (6) and oxygen ion transport anode[53]. Therefore, DRT curve of LSCF and LSCF cathode infiltrated with PNM5 consists of five peaks, which correspond to five processes of surface adsorption of oxygen (P_1), ORR process (P_2), oxygen ion transport in cathode (P_3), interfacial resistance between electrolyte (P_4) and cathode and ion transport

resistance in electrolyte (P_5), respectively. The rate-determining steps of cathode reaction is mainly ionic conduction and oxygen adsorption/desorption reactive process on cathode surface in the mixed electron-ionic materials. The DRT peak with the characteristic frequency of above 10 Hz describes oxygen transport in the open pore and in the catalyst layer, while the adsorption/desorption and ORR process occur at $\backsim$10Hz[54, 55]. This P_3 peak is the strongest, and it accounts for the largest proportion of total R_p value. According to deconvolution calculation of the DRT curve, this P_3 is actually an overlapping peak of several peaks, which means that it also includes two or three sub-processes, as shown in inset of LSCF at 973K and inset of LSCF infiltrated with PNM5 at 923K. Among peaks, P_1, P_2, P_3 and P_4 drift towards high frequency electrochemically with the increase in operation temperature, however P5 shows the opposite drift trend. For LSCF at 873K and 923K, P_3 peak corresponds to main resistance comes from the ORR process, and after operation temperature is increased to 973K due to the acceleration of the ORR process, the main resistance has been transferred to the diffusion and transport of oxygen ions in the cathode. The ORR process involves the reduction reaction in the gas-solid phase interface and in TPB. Of course, Ion transport also includes interface resistance between the PNM5 catalytic layer and the LSCF cathode and the transport resistance between the LSCF cathode. For the LSCF cathode infiltrated with PNM5, the peak P_3 mainly originates from oxygen ion diffusion and transport in cathode, and its corresponding frequency range from 10 to 100Hz. P_4 peak belongs to oxygen ion transport between LSCF and GDC electrolyte, the peak value decreases with the increase in operation temperature, it means that its proportion in the total R_p value decreases. However, P_5 value increases with the increase in operation temperature, indicating that the transport resistance of oxygen ions in the GDC electrolyte also increases. Obviously, ORR process increases with the increase in operation temperature. In comparation with Fig. (a) and Fig. (b), it is found that the total R_p value of the LSCF cathode infiltrated with PNM5 is significantly reduced. For LSCF infiltrated with PNM5 cathode, the intensity of the P_4 peak decreases

significantly with the increase of operation temperature. It shows that the proportion of the oxygen ion transport resistance between LSCF and GDC in the total R_p value decreases, revealing the increase in operation temperature has a more obvious impact on the rate of ion transport than on the ORR rate.

Firing temperature is an important factor for catalytic activity of PNM5. Fig.7(a) is Nyquist plots and equivalent circuit model of LSCF infiltrated with PNM5 at different firing temperature. R_∞ originates from electrolyte and electrodes. C_{chem} is a chemical bulk capacitance originated from oxygen stoichiometry variation in LSCF cathode layer. R_s is ORR progress resistance, this step represents the adsorption of oxygen from the air to the surface of the cathode particles, and then it is reduced and diffused to the vacancies in the surface of the particles. R_i indicates resistance of oxygen ion transport in LSCF infiltrated with PNM5, and Q is resistance constant phase element (CPE). R_b and C_b indicates resistance and capacitance of oxygen ion transport in GDC. This fitted R_p value is equal to the sum of R_s, R_i and R_b. The detailed fitting parameters of the equivalent circuit are shown in Table S1, indicating R_∞ value decreases and R_p value increases with the increase in firing temperature. R_b, R_i and R_s all increase with the increase in firing temperature, which directly leads to the increase of total resistance including R_∞ and R_p value increases. Shown in Fig.7(b) is a trend curve of total R_p value from symmetric cell calcined at a temperature range of 973K to 1173K, and the R_p originates from the equation $R_p = Z|_{\omega\to 0} - R_\infty$[56]. It is found that the R_p value decreases exponentially with decrease in firing temperature. At the same operating temperature, it can be seen that the higher the firing temperature, the greater the R_p value. To reveal the catalyst behavior of PNM5 further, the activation energy was calculated by the equation: $R_p = R_p^o\ (E_a/RT)$. Shown in Fig.7(c) is the plot of $\log_{10}(R_p)-1000/T$ and the corresponding activation energy for samples infiltrated with PNM5. The results show that activation energy is reduced from 1.77 to 1.45 eV when the infiltrated PNM5 sample was calcined at 1073K. Fig. 7(d) is DRT curve of LSCF infiltrated

with PNM5 samples, which were fired at 973, 1023, 1073, and 1123K temperature, respectively. It is found that the total R_p value increases with the increase in firing temperature. Xu et al. believe that the main reason is the increase in the transport resistance of oxygen ions between cathode and electrolyte[57]. Recrystallization caused by high temperature reduce the transport of oxygen ions[58]. However, the increase of the cathode backbone particles size reduces oxygen surface exchange of backbone particles, resulted in an increase in R_p value. The P_2 and P_3 peaks tend to drift towards low frequency with the increase in firing temperature, and it means ORR characteristic resistance accounts for an increase in the total R_p value, which indicates that the activity of the cathode catalytic layer decreases. Comparing the DRT curves of the LSCF cathode and LSCF cathode infiltrated with PNM5, it is found that the LSCF infiltrated PNM5 layer significantly reduces ORR process and oxygen ion transport resistance. But the firing temperature should not be too low. The first condition is to ensure that the PNM5 infiltration layer can be fired onto LSCF baseline layer, and then the most important requirement is obtaining the lowest activation energy. Therefore, the optimal firing temperature of LSCF cathode infiltrated with PNM5 is at 1073K.

The equivalent circuit fitted by ZSimpWin is shown in Fig.8(a), the fitted Nyquist plot as an example is shown in Fig. 8(b), and the corresponding fitting parameters are shown in Table 2. In these equivalent circuit model, *L* represents inductance due to electrode wire and Ag current collection network. When the R_p value is high, *L* cannot be displayed in the equivalent circuit due to the smaller inductance in the total R_p value. However, when the R_p value drops to a certain level, *L* occurs in the equivalent circuit. C_i is from grain boundary barrier of LSCF infiltrated with PNM5 cathode. When LSCF is at 973 and 1023K, the ion transport capacitance originating from the grain boundary barrier C_i is replaced by CPE-Q in the equivalent circuit, indicating ion transport resistance decreases due to the increase in operating temperature. ORR progress is related to the oxygen surface exchange coefficient k and the surface

diffusion coefficient D, and both k and D are positively correlated with temperature[12]. When the operating temperature is at 1023K, there is no C_{chem} and R_s of the surface ORR process in equivalent circuit of the LSCF infiltrated with PNM5. The main reason is that the surface ORR caused by the high temperature is faster and very small. It isn't displayed in the equivalent circuit, but it is not without ORR progress resistance. In the DRT function curve, the P_2 peak representing the ORR process is still obvious. R_b and C_b originates from resistance of oxygen ion transport in GDC, and it corresponds to P_4 and P_5 in the DRT curve. Obviously, the R_∞ and total R_p of LSCF cathode infiltrated with PNM5 are lower than that of blank LSCF due to surface modification. The total R_p and R_∞ both decrease with the increase in operation temperature. Transformation of equivalent circuit shows the nature of its dependence on temperature, and also reveals the evolution of resistance the oxygen ion transport process in oxide cell.

3.5 Performance of electrolyte-supported cell

Fig.9 is the R_p of LSCF infiltrated with PNM5 from symmetric cell as a function of operation time. The R_p value from LSCF infiltrated with PNM5 for ~ 200 h indicates an increase in R_p from 0.250 Ωcm^2 to 0.285 Ωcm^2 with an average degradation rate of 0.0217%. The R_p value of blank LSCF and LSCF infiltrated with PNM5 is obtained in a constant voltage of 0.012V. The degradation rate is the calculated slope according to linear fitting. In contrast, the average R_p value of the baseline LSCF is 0.443 Ωcm^2 with degradation rate of 0.0709%. The results show that LSCF infiltrated PNM5 not only has a significant enhancement in electrochemical activity for ORR progress, but also decreases the degradation rate of LSCF. To demonstrate the ORR activity of PNM5 catalyst furthermore, an electrolyte-supported cell with PNM5 catalyst infiltrated in the cathode was tested. Fig. 10 compares the performance of a baseline cell consisting of a standard NiO (65%) + GDC (35%) anode, GDC electrolyte and LSCF cathode with that of an PNM5-infiltrated cell that has other components the same as the baseline cell. The open circuit voltage (OCV) PNM5-infiltrated cell is 0.82 V at 1023K and decreases with the increase in current density

and operation temperature. Literature reported the OCV of LSCF is about 0.9-1.1V, but low density of electrolyte or gas leakage reduces the OCV value[59]. But it is noted that infiltrated process has no effect on the OCV value. The results indicate the maximum power density increases with the increase in operation temperature. However, the peak power densities were 0.0241 W/cm^2 for the blank cell and 0.058 W/cm^2 for the infiltrated cell, it is evident that the infiltrated cell exhibits an increase of higher peak power density with an average 140.66 percentage than the baseline cell.

Above results show that LSCF infiltrated with PNM5 catalytic layer can effectively improve cell surface ORR. LSCF infiltrated with PNM5 thin layer is only of 50-70nm thickness, and thin layer composed of nano-particles have a huge gas-solid interface reactive area and more TPB, which is a significant reason for reducing R_∞ and R_p value. PNM5 is an effective catalytic multi-phase materials composed of MnO, NiO and Pr_6O_{11}, and this multi-phase system has significant advantages in preventing diffusion and growth of particle size and stabilizing the surface reaction area in gas-solid interface and TPB[60]. So, it is of positive significance for stabilizing the ORR process and ion transport efficiency in LSCF cathode. The enhanced activity of the porous cathode is mainly derived from the porous granular structure. These large two-phase and three-phase regions reduce the diffusion resistance of oxygen and promote ORR process. Moreover, increasing oxygen reaction contact area between LSCF particle and gas is an effective pathway to enhance the ORR process [19]. Sr surface segregation on LSCF depends on surface orientation and humidity of the air[61, 62]. Therefore, the biggest challenge to the long-term operation of LSCF cathode is the degradation of the ORR process due to surface Sr segregation, and it caused the deterioration and decomposition of the porous perovskite phase backbone [63]. So, it is a key issue need to be resolved to suppress the surface Sr segregation in LSCF and enhance the surface ORR and reducing the operating temperature. Enhanced long-term stability of LSCF infiltrated with PNM5 may be related to the suppression of Sr surface segregation.

Ⅳ. Conclusions

In conclusion, LSCF cathodes surface modified by nano-sized PNM5 particles were successfully fabricated by a multi-step infiltration method, producing uniformly distributed PNM5 nanoscale film and nano-particles on the surface of LSCF grains. The PNM5 infiltrated LSCF cathodes showed appreciably lower R_p value than the baseline LSCF cathodes. The microstructures and performances of PNM5 infiltrated cathodes depend sensitively on the amount of PNM5 introduced and the microstructure of the PNM5 coatings controlled by firing temperature. For the LSCF cathode infiltrated with 0.25 mol L^{-1} PNM5, the R_p value is about half the baseline cathode. Furthermore, the infiltrated symmetric cell showed an improved stability within the time than blank LSCF although the detailed mechanism is yet to be determined. LSCF infiltrated with PNM5 has a significant dependence on temperature, the ORR resistance of the cathode surface increases with the increase of firing temperature, while the increase of operating temperature significantly reduces the R_p value and R_∞ value. The performance of cells infiltrated with PNM5 show an increase of 140.66% higher than the baseline cell. These results indicated PNM5 as a potential catalytic enhancer for boosting ORR progress for commercial LSCF cathodes.

Acknowledgment

The work was supported by the U. S. department of energy under award number of DE-AR-0000492. Dr Tao Wei and Dr Cuijuan Zhang gave some helps for this paper, the authors are grateful to them.

References

[1] K.D. Kreuer, S.J. Paddison, E. Spohr, M. Schuster, Transport in proton conductors for fuel-cell applications: Simulations, elementary reactions, and phenomenology, Chemical Reviews 104(10) (2004) 4637-4678.

[2] I. Savych, S. Subianto, Y. Nabil, S. Cavaliere, D. Jones, J. Roziere, Negligible degradation upon in situ voltage cycling of a PEMFC using an electrospun niobium-doped tin oxide supported Pt cathode, Phys Chem Chem Phys 17(26) (2015) 16970-16976.

[3] S.J. Bae, Y. Ahn, J. Lee, J.I. Lee, Various supercritical carbon dioxide cycle layouts study for molten carbonate fuel cell application, J Power Sources 270 (2014) 608-618.

[4] M.L. Liu, M.E. Lynch, K. Blinn, F.M. Alamgir, Y. Choi, Rational SOFC material design: new advances and tools, Mater Today 14(11) (2011) 534-546.

[5] M. Singh, D. Zappa, E. Comini, Solid oxide fuel cell: Decade of progress, future perspectives and challenges, Int J Hydrogen Energ 46(54) (2021) 27643-27674.

[6] M.H.D. Othman, N. Droushiotis, Z.T. Wu, G. Kelsall, K. Li, High-Performance, Anode-Supported, Microtubular SOFC Prepared from Single-Step-Fabricated, Dual-Layer Hollow Fibers, Advanced Materials 23(21) (2011) 2480-2483.

[7] T. Wei, P. Singh, Y.H. Gong, J.B. Goodenough, Y.H. Huang, K. Huang, Sr3-3xNa3xSi3O9-1.5x (x=0.45) as a superior solid oxide-ion electrolyte for intermediate temperature-solid oxide fuel cells, Energ Environ Sci 7(5) (2014) 1680-1684.

[8] Y.R. Wang, Z.B. Yang, F.L. Lu, C. Jin, J. Wu, M. Shen, R.Z. Yang, F.L. Chen, Carbon-coating functionalized La0.6Sr1.4MnO4+delta layered perovskite oxide: enhanced catalytic activity for the oxygen reduction reaction, Rsc Adv 5(2) (2015) 974-980.

[9] E. Dogdibegovic, R. Wang, G.Y. Lau, A. Karimaghaloo, M.H. Lee, M.C. Tucker, Progress in durability of metal-supported solid oxide fuel cells with infiltrated electrodes, J Power Sources 437 (2019) 226935.

[10] J.M. Vohs, R.J. Gorte, High-Performance SOFC Cathodes Prepared by Infiltration, Advanced Materials 21(9) (2009) 943-956.

[11] L.F. Nie, M.F. Liu, Y.J. Zhang, M.L. Liu, La0.6Sr0.4Co0.2Fe0.8O3-delta cathodes infiltrated with samarium-doped cerium oxide for solid oxide fuel cells, J Power Sources 195(15) (2010) 4704-4708.

[12] S.P. Jiang, Development of lanthanum strontium cobalt ferrite perovskite electrodes of solid oxide fuel cells – A review, Int J Hydrogen Energ 44(14) (2019) 7448-7493.

[13] F.S. Baumann, J. Fleig, H.-U. Habermeier, J. Maier, Impedance spectroscopic study on well-defined (La,Sr)(Co,Fe)O3−δ model electrodes, Solid State Ionics 177(11) (2006) 1071-1081.

[14] A. Esquirol, N.P. Brandon, J.A. Kilner, M. Mogensen, Electrochemical Characterization of La[sub 0.6]Sr[sub 0.4]Co[sub 0.2]Fe[sub 0.8]O[sub 3] Cathodes for Intermediate-Temperature SOFCs, J Electrochem Soc 151(11) (2004) A1847.

[15] L.W. Tai, M.M. Nasrallah, H.U. Anderson, D.M. Sparlin, S.R. Sehlin, Structure and electrical properties of La1 − xSrxCo1 − yFeyO3. Part 2. The system La1 − xSrxCo0.2Fe0.8O3, Solid State Ionics 76(3) (1995) 273-283.

[16] L.W. Tai, M.M. Nasrallah, H.U. Anderson, D.M. Sparlin, S.R. Sehlin, Structure and electrical properties of La1−xSrxCo1−yFeyO3. Part 1. The system La0.8Sr0.2Co1−yFeyO3, Solid State Ionics 76(3) (1995) 259-271.

[17] B. Fan, J. Yan, X. Yan, The ionic conductivity, thermal expansion behavior, and chemical compatibility of La0.54Sr0.44Co0.2Fe0.8O3-δ as SOFC cathode material, Solid State Sci 13(10) (2011) 1835-1839.

[18] S.A. Muhammed Ali, M. Anwar, N.A. Baharuddin, M.R. Somalu, A. Muchtar, Enhanced electrochemical performance of LSCF cathode through selection of optimum fabrication parameters, J Solid State Electr 22(1) (2018) 263-273.

[19] I. Jang, S. Kim, C. Kim, H. Yoon, T. Song, Enhancement of oxygen reduction reaction through coating a nano-web-structured La0.6Sr0.4Co0.2Fe0.8O3-δ thin-film as a cathode/electrolyte interfacial layer for lowering the operating temperature of solid oxide fuel cells, J Power Sources 392 (2018) 123-128.

[20] Y. Liu, X. Meng, F. Yu, M. Yin, N. Yang, B. Meng, M.V. Sofianos, S. Liu, Enhancing oxygen reduction reaction activity of perovskite oxides cathode for solid oxide fuel cells using a novel anion doping strategy, Int J Hydrogen Energ 43(27) (2018) 12328-12336.

[21] Y.-P. Wang, S.-H. Liu, H.-Y. Zhang, C.-X. Li, S.-L. Zhang, G.-J. Yang, C.-J. Li, Structured La0.6Sr0.4Co0.2Fe0.8O3-δ cathode with large-scale vertical cracks by atmospheric laminar plasma spraying for IT-SOFCs, J Alloy Compd 825 (2020) 153865.

[22] A.E. Mejía Gómez, J. Sacanell, C. Huck-Iriart, C.P. Ramos, A.L. Soldati, S.J.A. Figueroa, M.H. Tabacniks, M.C.A. Fantini, A.F. Craievich, D.G. Lamas, Crystal structure, cobalt and iron speciation and oxygen non-stoichiometry of La0.6Sr0.4Co1-yFeyO3-δ nanorods for IT-SOFC cathodes, J Alloy Compd 817 (2020) 153250.

[23] G. Li, B. He, Y. Ling, J. Xu, L. Zhao, Highly active YSB infiltrated LSCF cathode for proton conducting solid oxide fuel cells, Int J Hydrogen Energ 40(39) (2015) 13576-13582.

[24] X. Lou, S. Wang, Z. Liu, L. Yang, M. Liu, Improving La0.6Sr0.4Co0.2Fe0.8O3−δ cathode performance by infiltration of a Sm0.5Sr0.5CoO3−δ coating, Solid State Ionics 180(23) (2009) 1285-1289.

[25] D. Ding, X.X. Li, S.Y. Lai, K. Gerdes, M.L. Liu, Enhancing SOFC cathode performance by surface modification through infiltration, Energ Environ Sci 7(2) (2014) 552-575.

[26] M.E. Lynch, L. Yang, W.T. Qin, J.J. Choi, M.F. Liu, K. Blinn, M.L. Liu, Enhancement of La0.6Sr0.4Co0.2Fe0.8O3-delta durability and surface electrocatalytic activity by La0.85Sr0.15MnO3 +/-delta investigated using a new test electrode platform, Energ Environ Sci 4(6) (2011) 2249-2258.

[27] N.K. Patel, R.G. Utter, D. Das, M. Pecht, Surface degradation of strontium-based perovskite electrodes of solid oxide fuel cells, J Power Sources 438 (2019) 227040.

[28] L. Wang, R. Merkle, Y.A. Mastrikov, E.A. Kotomin, J. Maier, Oxygen exchange kinetics on solid oxide fuel cell cathode materials—general trends and their mechanistic interpretation, J Mater Res 27(15) (2012) 2000-2008.

[29] T. Hong, L. Zhang, F. Chen, C. Xia, Oxygen surface exchange properties of La0.6Sr0.4Co0.8Fe0.2O3 − δ coated with SmxCe1 − xO2 − δ, J Power Sources 218 (2012) 254-260.

[30] X.G. Cao, S.P. Jiang, Oxygen reduction reaction at (La,Sr) (Co,Fe)O3-δ electrode/La9.5Si6O26.25 apatite electrolyte interface of solid oxide fuel cells, Int J Hydrogen Energ 41(2) (2016) 1203-1212.

[31] S.I. Hashimoto, K. Kammer, P.H. Larsen, F.W. Poulsen, M. Mogensen, A study of Pr0.7Sr0.3Fe1-xNixO3-delta as a cathode material for SOFCs with intermediate operating temperature, Solid State Ionics 176(11-12) (2005) 1013-1020.

[32] J. Dailly, S. Fourcade, A. Largeteau, F. Mauvy, J.C. Grenier, M. Marrony, Perovskite and A(2)MO(4)-type oxides as new cathode materials for protonic solid oxide fuel cells, Electrochim Acta 55(20) (2010) 5847-5853.

[33] Q. Zhou, L. Qu, T. Zhang, Y. He, C. Zhao, M. Wang, T. Wei, Y. Zhang, Preparation and electrochemical properties of an La-doped Pr2Ni0.85Cu0.1Al0.05O4+δ cathode material for an IT-SOFC, J Alloy Compd 824 (2020) 153967.

[34] V.V. Kharton, A.P. Viskup, A.V. Kovalevsky, E.N. Naumovich, F.M.B. Marques, Ionic transport in oxygen-hyperstoichiometric phases with K2NiF4-type structure, Solid State Ionics 143(3-4) (2001) 337-353.

[35] J. Dailly, F. Mauvy, M. Marrony, M. Pouchard, J.C. Grenier, Electrochemical properties of perovskite and A(2)MO(4)-type oxides used as cathodes in protonic ceramic half cells, J Solid State Electr 15(2) (2011) 245-251.

[36] A. Montenegro-Hernandez, J. Vega-Castillo, L. Mogni, A. Caneiro, Thermal stability of Ln(2)NiO(4+delta) (Ln: La, Pr, Nd) and their chemical compatibility with YSZ and CGO solid electrolytes, Int J Hydrogen Energ 36(24) (2011) 15704-15714.

[37] S.S. Bhoga, A.P. Khandale, B.S. Pahune, Investigation on Pr-2 (-) xSrxNiO4 (+) (delta) (x=0.3-1.0) cathode materials for intermediate temperature solid oxide fuel cell, Solid State Ionics 262 (2014) 340-344.

[38] B.S. Kang, A. Inoishi, A. Takagaki, T. Ishihara, Pr2Ni0.71Cu0.24Ga0.05O4-Sm0.2Ce0.8O1.9 composite film as active cathodic layer for intermediate temperature solid oxide fuel cells, Solid State Ionics 327 (2018) 59-63.

[39] C.G. Moura, J.P.d.F. Grilo, D.A. Macedo, M.R. Cesário, D.P. Fagg, R.M. Nascimento, Cobalt-free perovskite Pr0.5Sr0.5Fe1−xCuxO3−δ (PSFC) as a cathode material for intermediate temperature solid oxide fuel cells, Mater Chem Phys 180 (2016) 256-262.

[40] J. Mao, S. Peng, C. Zhang, S. Qi, J. Cui, Y. Gong, S. Wang, C. Wu, Q. Zhou, Electrode properties of (Pr0.9La0.1)2−x(Ni0.74Cu0.21Al0.05)O4+δ (with x=0, 0.05, and 0.1) as cathodes in IT-SOFCs, J Alloy Compd 793 (2019) 519-525.

[41] T. Reshetenko, A. Kulikovsky, Distribution of Relaxation Times: A Tool for Measuring Oxygen Transport Resistivity of a Low–Pt PEM Fuel Cell Cathode, J Electrochem Soc 167(14) (2020) 144505.

[42] F. Ciucci, C. Chen, Analysis of Electrochemical Impedance Spectroscopy Data Using the Distribution of Relaxation Times: A Bayesian and Hierarchical Bayesian Approach, Electrochim Acta 167 (2015) 439-454.

[43] M. Castro, R. Burriel, Heat capacity study of La2NiO4 and Pr2NiO4, Thermochim Acta 269 (1995) 537-552.

[44] S. Miyoshi, T. Furuno, H. Matsumoto, T. Ishihara, Conductivity and oxygen permeability of a novel oxide Pr2Ni0.8-xCu0.2FexO4 and its application to partial oxidation of CH4, Solid State Ionics 177(26-32) (2006) 2269-2273.

[45] P. Lacorre, J.B. Torrance, J. Pannetier, A.I. Nazzal, P.W. Wang, T.C. Huang, Synthesis, crystal structure, and properties of metallic PrNiO3: Comparison with metallic NdNiO3 and semiconducting SmNiO3, J Solid State Chem 91(2) (1991) 225-237.

[46] V. Vibhu, A. Flura, C. Nicollet, S. Fourcade, N. Penin, J.-M. Bassat, J.-C. Grenier, A. Rougier, M. Pouchard, Characterization of PrNiO3-δ as oxygen electrode for SOFCs, Solid State Sci 81 (2018) 26-31.

[47] M.F. Gazulla, M.J. Ventura, C. Andreu, J. Gilabert, M. Orduña, M. Rodrigo, Praseodymium oxides. Complete characterization by determining oxygen content, Microchemical Journal 148 (2019) 291-298.

[48] A. Netz, W.F. Chu, V. Thangadurai, R.A. Huggins, W. Weppner, Investigations of praseodymium oxide electrodes in lithium concentration cells, Ionics 5(5) (1999) 426-433.

[49] D. Ding, X. Li, S.Y. Lai, K. Gerdes, M. Liu, Enhancing SOFC cathode performance by surface modification through infiltration, Energ Environ Sci 7(2) (2014) 552-575.

[50] B.M. Abu-Zied, Controlled synthesis of praseodymium oxide nanoparticles obtained by combustion route: Effect of calcination temperature and fuel to oxidizer ratio, Appl Surf Sci 471 (2019) 246-255.

[51] M. Shamshi Hassan, M. Shaheer Akhtar, K.-B. Shim, O.B. Yang, Morphological and Electrochemical Properties of Crystalline Praseodymium Oxide Nanorods, Nanoscale Res Lett 5(4) (2010) 735.

[52] W. Carrillo-Cabrera, J.B. Wagner, The effect of high temperature pre-annealing on the electrical conductivity of polycrystalline nickel oxide at intermediate temperatures, Solid State Ionics 28-30 (1988) 1396-1401.

[53] X. Ding, X. Zhao, Y. Yan, M. Li, Enhancing oxygen reduction activity of perovskite cathode decorated with core@shell nano catalysts, Int J Hydrogen Energ 44(39) (2019) 22122-22128.

[54] H. Sumi, T. Yamaguchi, K. Hamamoto, T. Suzuki, Y. Fujishiro, High performance of La0.6Sr0.4Co0.2Fe0.8O3–Ce0.9Gd0.1O1.95 nanoparticulate cathode for intermediate temperature microtubular solid oxide fuel cells, J Power Sources 226 (2013) 354-358.

[55] H. Sumi, H. Shimada, Y. Yamaguchi, Y. Mizutani, Y. Okuyama, K. Amezawa, Comparison of electrochemical impedance spectra for electrolyte-supported solid oxide fuel cells (SOFCs) and protonic ceramic fuel cells (PCFCs), Sci Rep-Uk 11(1) (2021) 10622.
[56] A. Kulikovsky, PEM fuel cell distribution of relaxation times: a method for the calculation and behavior of an oxygen transport peak, Phys Chem Chem Phys 22(34) (2020) 19131-19138.
[57] H. Xu, H. Zhang, A. Chu, An investigation of oxygen reduction mechanism in nano-sized LSCF-SDC composite cathodes, Int J Hydrogen Energ 41(47) (2016) 22415-22421.
[58] Đ. Tripković, R. Küngas, M.B. Mogensen, P.V. Hendriksen, Surface recrystallization – an underestimated phenomenon affecting oxygen exchange activity, J Mater Chem A 7(19) (2019) 11782-11791.
[59] K. Chen, X. Chen, Z. Lü, N. Ai, X. Huang, W. Su, Performance of an anode-supported SOFC with anode functional layers, Electrochim Acta 53(27) (2008) 7825-7830.
[60] Y. Niu, Y. Zhou, W. Lv, Y. Chen, Y. Zhang, W. Zhang, Z. Luo, N. Kane, Y. Ding, L. Soule, Y. Liu, W. He, M. Liu, Enhancing Oxygen Reduction Activity and Cr Tolerance of Solid Oxide Fuel Cell Cathodes by a Multiphase Catalyst Coating, 31(19) (2021) 2100034.
[61] K. Develos-Bagarinao, J. De Vero, H. Kishimoto, T. Ishiyama, K. Yamaji, T. Horita, H. Yokokawa, Oxygen surface exchange properties and surface segregation behavior of nanostructured La0.6Sr0.4Co0.2Fe0.8O3−δ thin film cathodes, Phys Chem Chem Phys 21(13) (2019) 7183-7195.
[62] M. Niania, R. Podor, T.B. Britton, C. Li, S.J. Cooper, N. Svetkov, S. Skinner, J. Kilner, In situ study of strontium segregation in La0.6Sr0.4Co0.2Fe0.8O3−δ in ambient atmospheres using high-temperature environmental scanning electron microscopy, J Mater Chem A 6(29) (2018) 14120-14135.
[63] Y. Chen, S.A. Paredes-Navia, C.-O. Romo-De-La-Cruz, L. Liang, A. Fernandes, A. Hinerman, J. Prucz, M. Williams, X. Song, Coating internal surface of porous electrode for decreasing the ohmic resistance and shifting oxygen reduction reaction pathways in solid oxide fuel cells, J Power Sources 499 (2021) 229854.

Caption

Fig. 1 (A)XRD patterns of PNM powder with different Manganese content, the powder was made at 1073K. ICSD numbers are NiO (221189), Pr_6O_{11} (421121), PrO_2 (750152), $PrNiO_3$ (801945) and MnO (750257). (B) XRD patterns of LSCF powder and LSCF powder with infiltration of PNM5, the powder was made at 1073K.

Fig. 2 Cross section morphology of LSCF cathode: (A)overall view of LSCF cathode; (B) morphology of LSCF infiltrated with PNM5; (C)magnified morphology of LSCF; (D) magnified morphology of LSCF infiltrated with PNM5; (E) magnified morphology of LSCF after a stability operation temperature at 973K for 200 hours; (F) magnified morphology of LSCF infiltrated with PNM5 after a stability operation temperature at 973K for 200 hours.

Fig.3 TEM and STEM mapping figure LSCF cathode with infiltration of PNM5. a. TEM picture; b. STEM energy spectrum picture, the inset indicates the area where the energy spectrum is obtained; c-i is in turn STEM mapping figure of La, Sr, Co, Fe, O, Pr, Ni.

Fig. 4 Temperature dependences of total electrical conductivity of the PNM samples.

Fig. 5 (A)Impedance spectra of LSCF symmetrical cell cathodes infiltrated with Pr-Ni-Mn oxides at 1023K, volume of infiltration species is at 21 microliter, infiltration spices were fired at 1173K for 1 hour. (B) Impedance spectra of LSCF symmetrical cell cathodes infiltrated with different phase at 1023K, infiltration spices were fired at 1173K for 1 hour. (C) Impedance spectra of LSCF symmetrical cell cathodes infiltrated with PNM5, infiltration solution is of different concentration at 923K, infiltration spices were fired at 1073K for 1 hour.

Fig. 6 DRT curves of blank LSCF and LSCF infiltrated with PNM5 at different operation temperature: (A) blank LSCF; (B) LSCF infiltrated with PNM5.

Fig. 7 (A) The Nyquist plots and equivalent circuit model of LSCF cathodes infiltrated with PNM5 samples at different fired temperature; (B) The R_p of LSCF infiltrated with PNM5 at a fired temperature ranged from 973K to 1173K. (C) $Lg(R_p) - 1000/T$ and activation energy of LSCF symmetrical cell infiltrated with PNM5. (D) DRT curves of LSCF infiltrated with PNM5 samples at different fired temperature at an operation temperature of 923K.

Fig. 8 (A)The equivalent circuit model of LSCF infiltrated with PNM5 and blank LSCF for fitting the obtained experimental data of EIS at an operation temperature ranged from 873K to 1023K by ZSimpWin software, and the subscript s represents the surface oxygen reduction reaction, i represents the ion transport from

LSCF cathode to GDC; b represents the bulk GDC electrolyte. (B) The Nyquist plots of LSCF and LSCF infiltrated with PNM5 operated at 1023K;

Fig.9 The R_p value of LSCF infiltrated with PNM5 from symmetric cell as a function of operation time.

Fig.10 I-V and power density of LSCF cell under H_2/Air (A) and I-V and power density of LSCF cell infiltrated with PNM5 under H_2/Air (B)

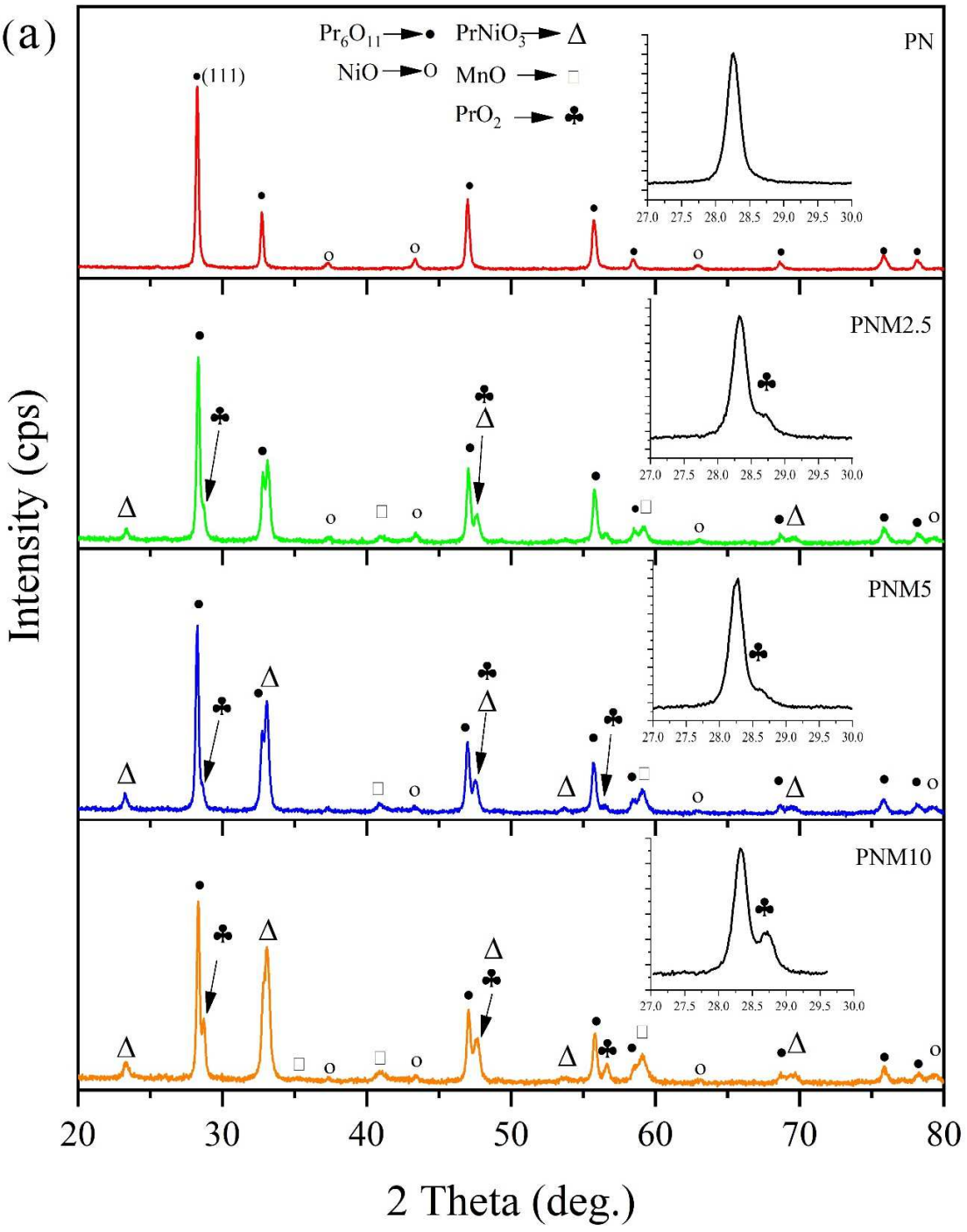
(a)
Pr_6O_{11} → •
NiO → o
$PrNiO_3$ → Δ
MnO → □
PrO_2 → ♣
•(111)
PN
PNM2.5
PNM5
PNM10
Intensity (cps)
2 Theta (deg.)
20
30
40
50
60
70
80
27.0
27.5
28.0
28.5
29.0
29.5
30.0

Fig.1 (a)

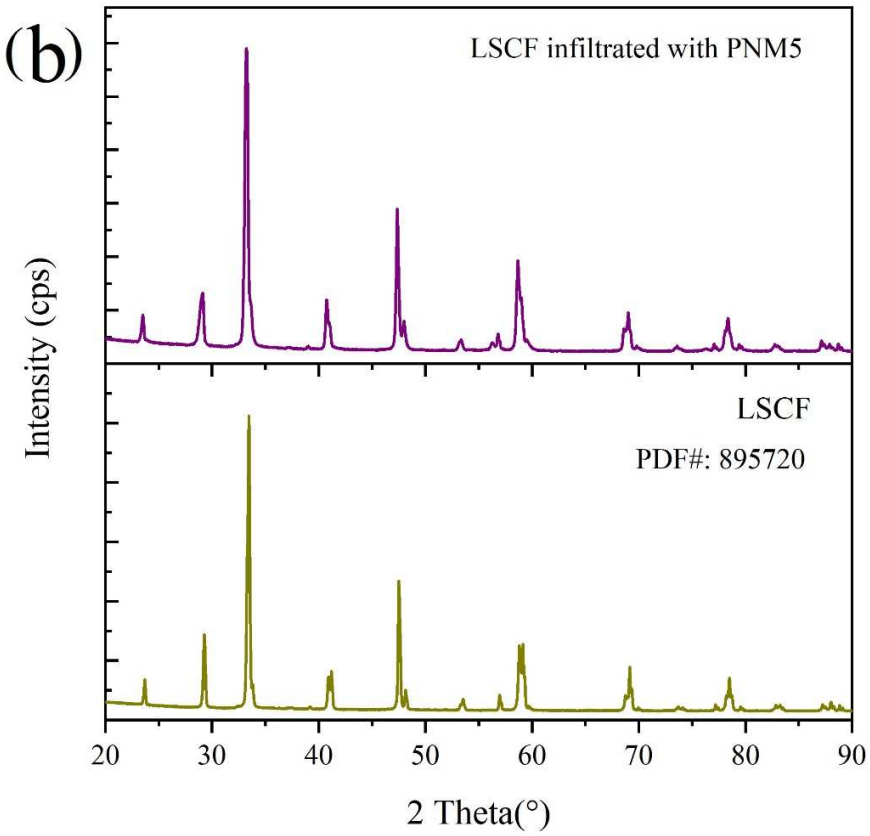
(b)
LSCF infiltrated with PNM5
LSCF
PDF#: 895720
Intensity (cps)
20
30
40
50
60
70
80
90
2 Theta(°)

Fig.1 (b)

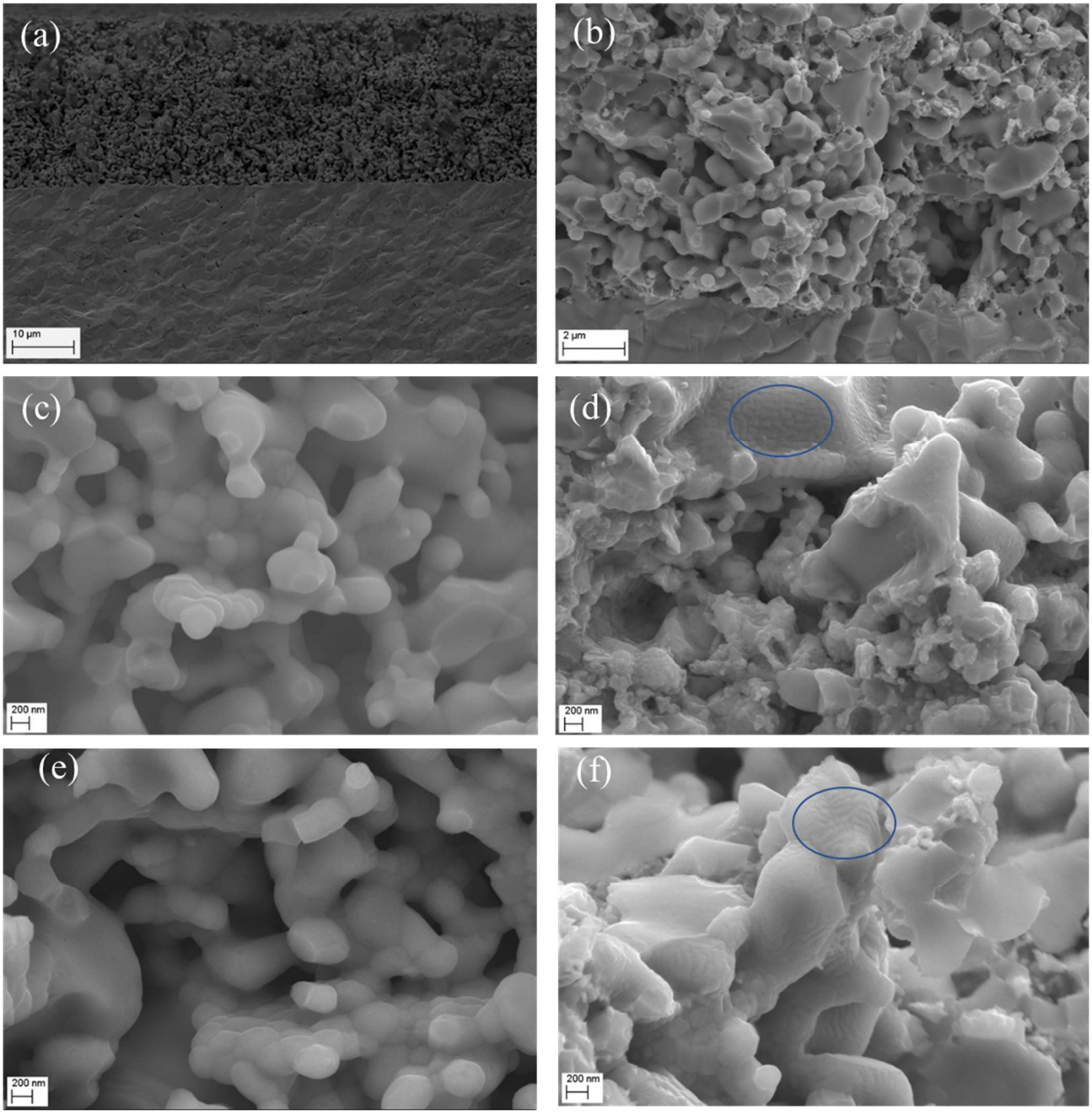

Fig. 2

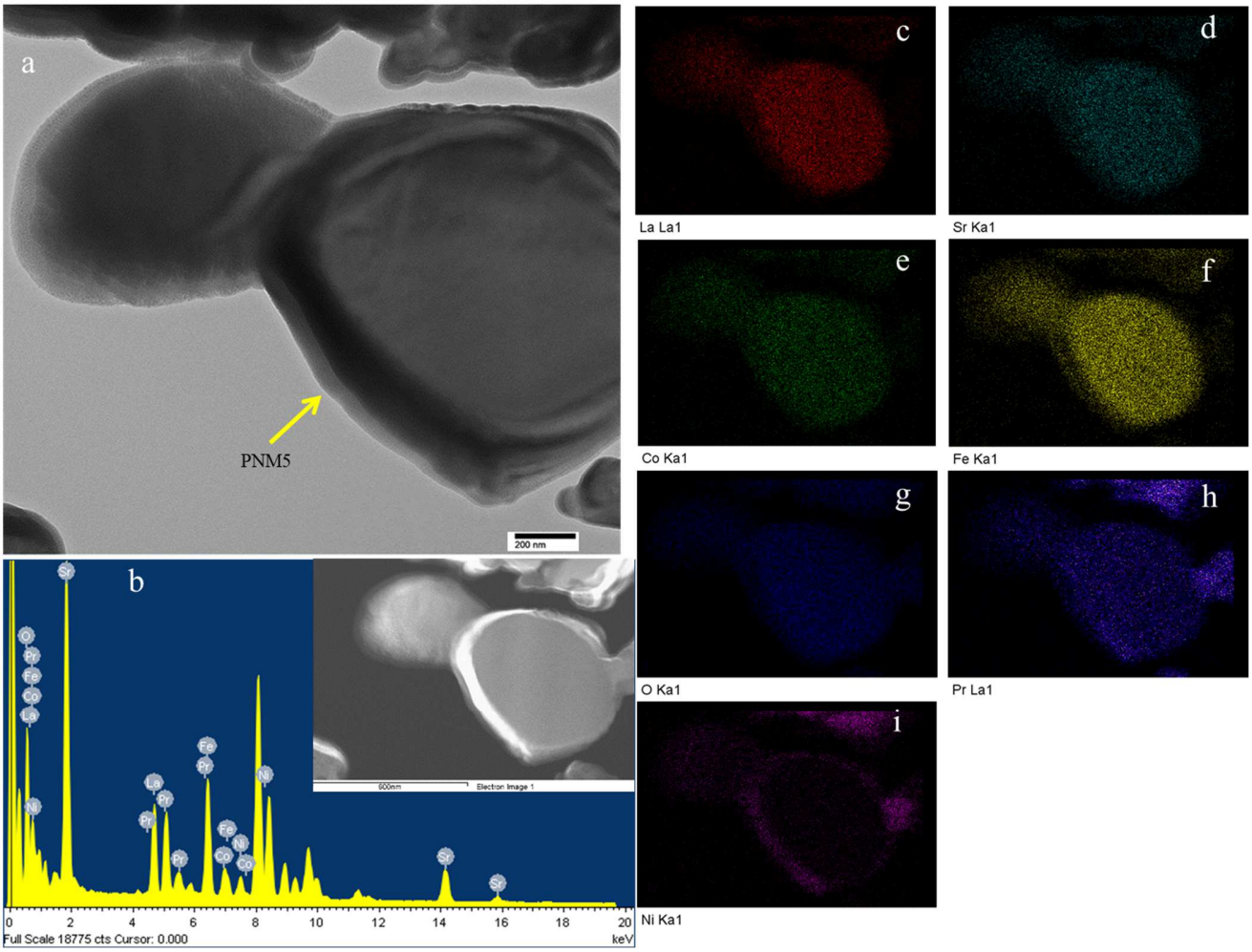
a
PNM5
200 nm
b
Sr
O
Pr
Fe
Co
La
Ni
Full Scale 18775 cts Cursor: 0.000
keV
c
La La1
d
Sr Ka1
e
Co Ka1
f
Fe Ka1
g
O Ka1
h
Pr La1
i
Ni Ka1

Fig.3

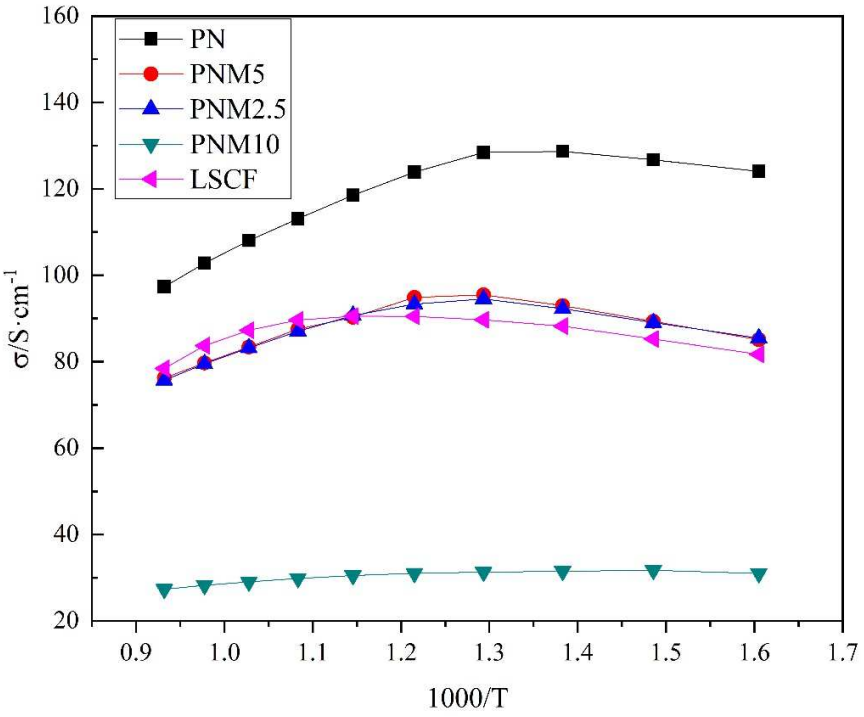
PN
PNM5
PNM2.5
PNM10
LSCF
σ/S·cm-1
1000/T
160
140
120
100
80
60
40
20
0.9
1.0
1.1
1.2
1.3
1.4
1.5
1.6
1.7

Fig. 4

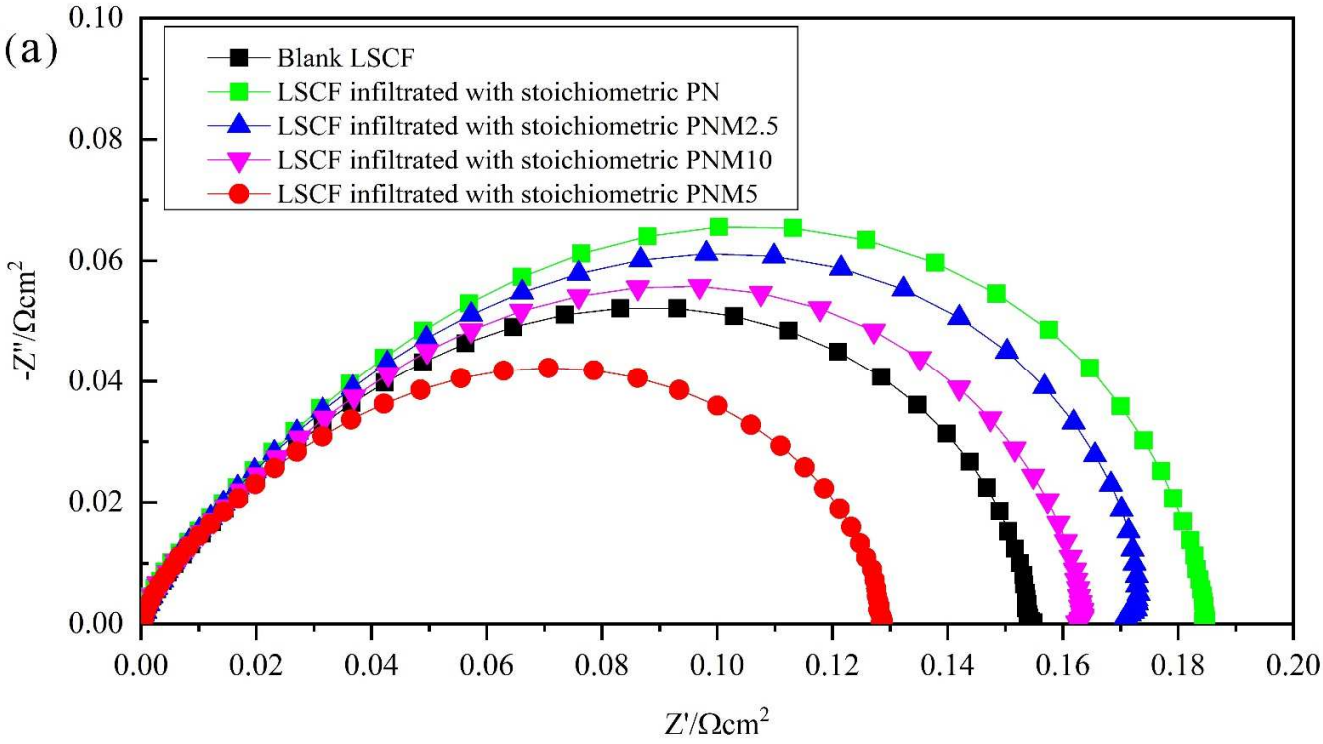
(a)
Blank LSCF
LSCF infiltrated with stoichiometric PN
LSCF infiltrated with stoichiometric PNM2.5
LSCF infiltrated with stoichiometric PNM10
LSCF infiltrated with stoichiometric PNM5
-Z''/Ωcm2
Z'/Ωcm2
0.10
0.08
0.06
0.04
0.02
0.00
0.00
0.02
0.04
0.06
0.08
0.10
0.12
0.14
0.16
0.18
0.20

Fig. 5 (A)

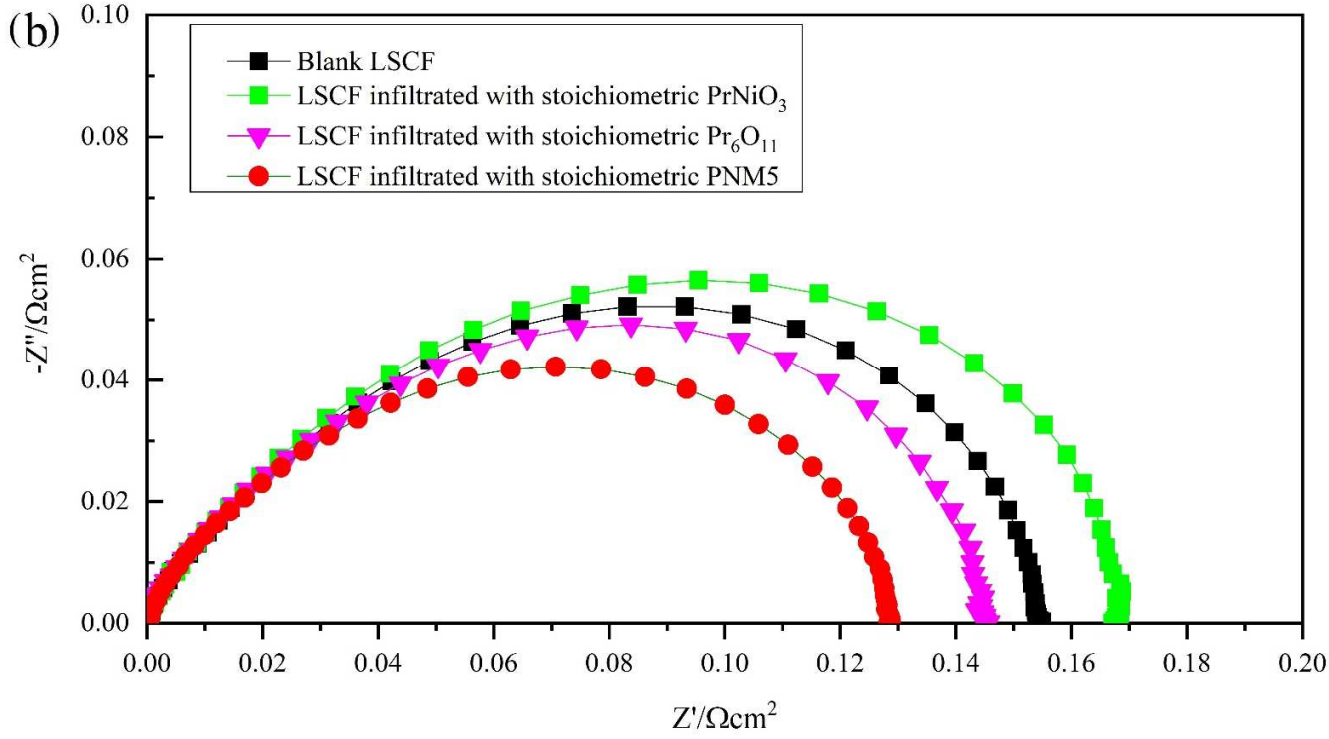
(b)
Blank LSCF
LSCF infiltrated with stoichiometric PrNiO3
LSCF infiltrated with stoichiometric Pr6O11
LSCF infiltrated with stoichiometric PNM5
-Z''/Ωcm2
Z'/Ωcm2
0.00
0.02
0.04
0.06
0.08
0.10
0.12
0.14
0.16
0.18
0.20

Fig. 5 (B)

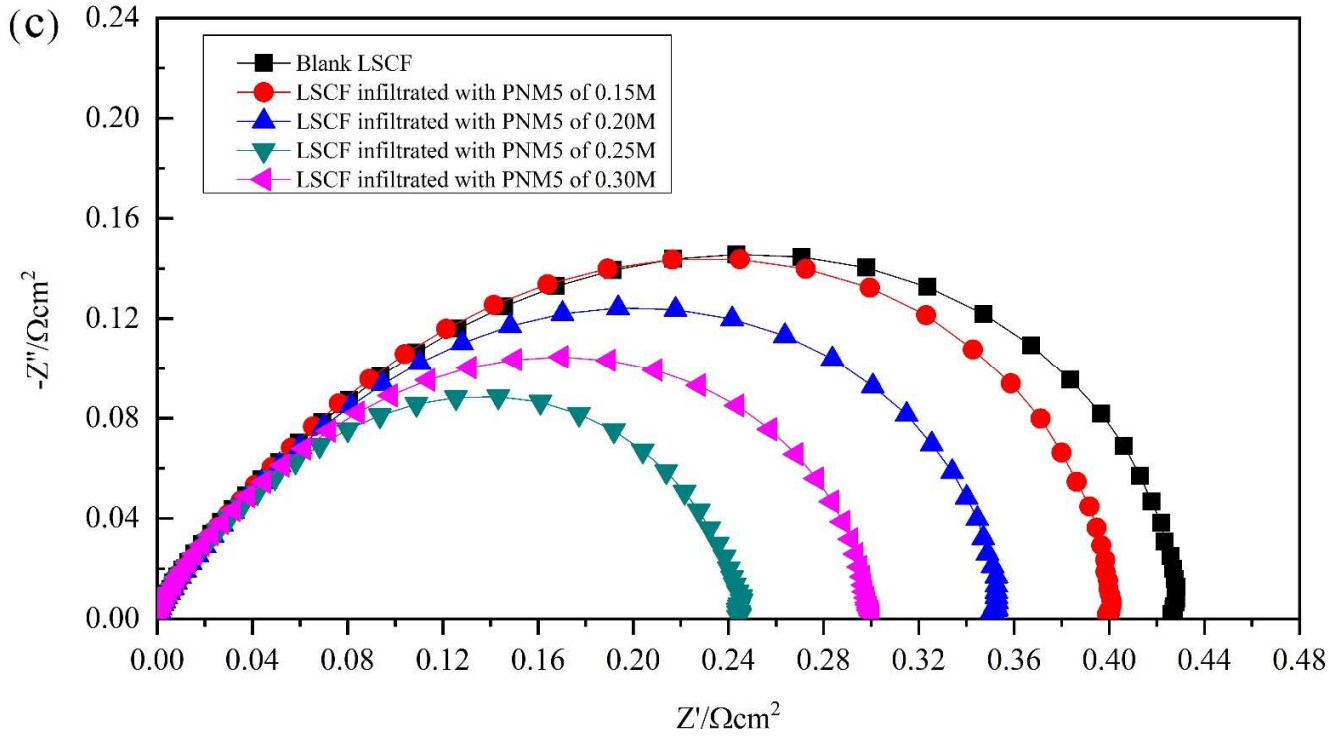
(c)
Blank LSCF
LSCF infiltrated with PNM5 of 0.15M
LSCF infiltrated with PNM5 of 0.20M
LSCF infiltrated with PNM5 of 0.25M
LSCF infiltrated with PNM5 of 0.30M
-Z''/Ωcm2
Z'/Ωcm2
0.00
0.04
0.08
0.12
0.16
0.20
0.24
0.28
0.32
0.36
0.40
0.44
0.48

Fig. 5 (C)

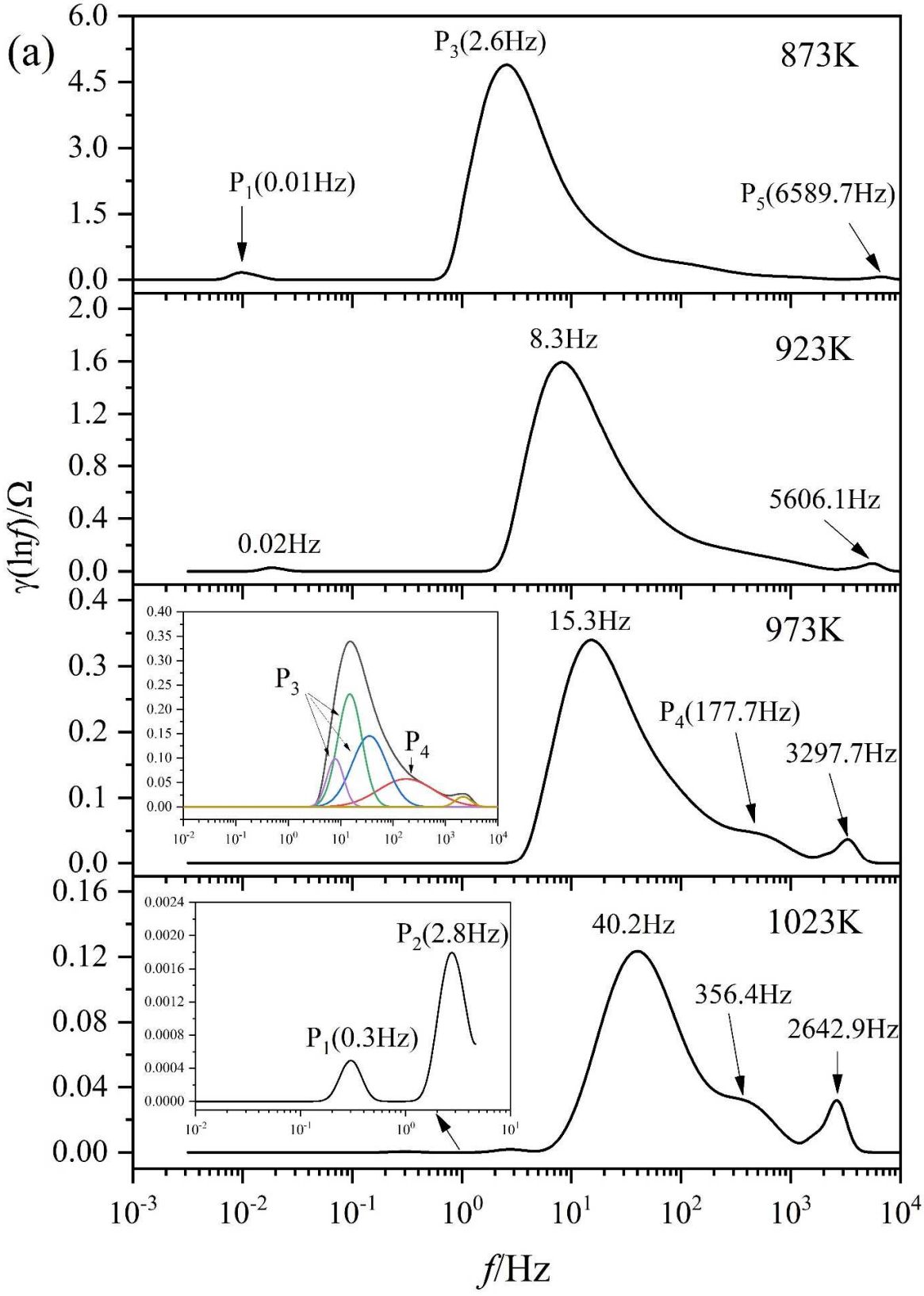
(a)
873K
P3(2.6Hz)
P1(0.01Hz)
P5(6589.7Hz)
923K
8.3Hz
0.02Hz
5606.1Hz
973K
15.3Hz
P4(177.7Hz)
3297.7Hz
P3
P4
1023K
40.2Hz
P2(2.8Hz)
P1(0.3Hz)
356.4Hz
2642.9Hz
γ(lnf)/Ω
f/Hz

Fig. 6 (A)

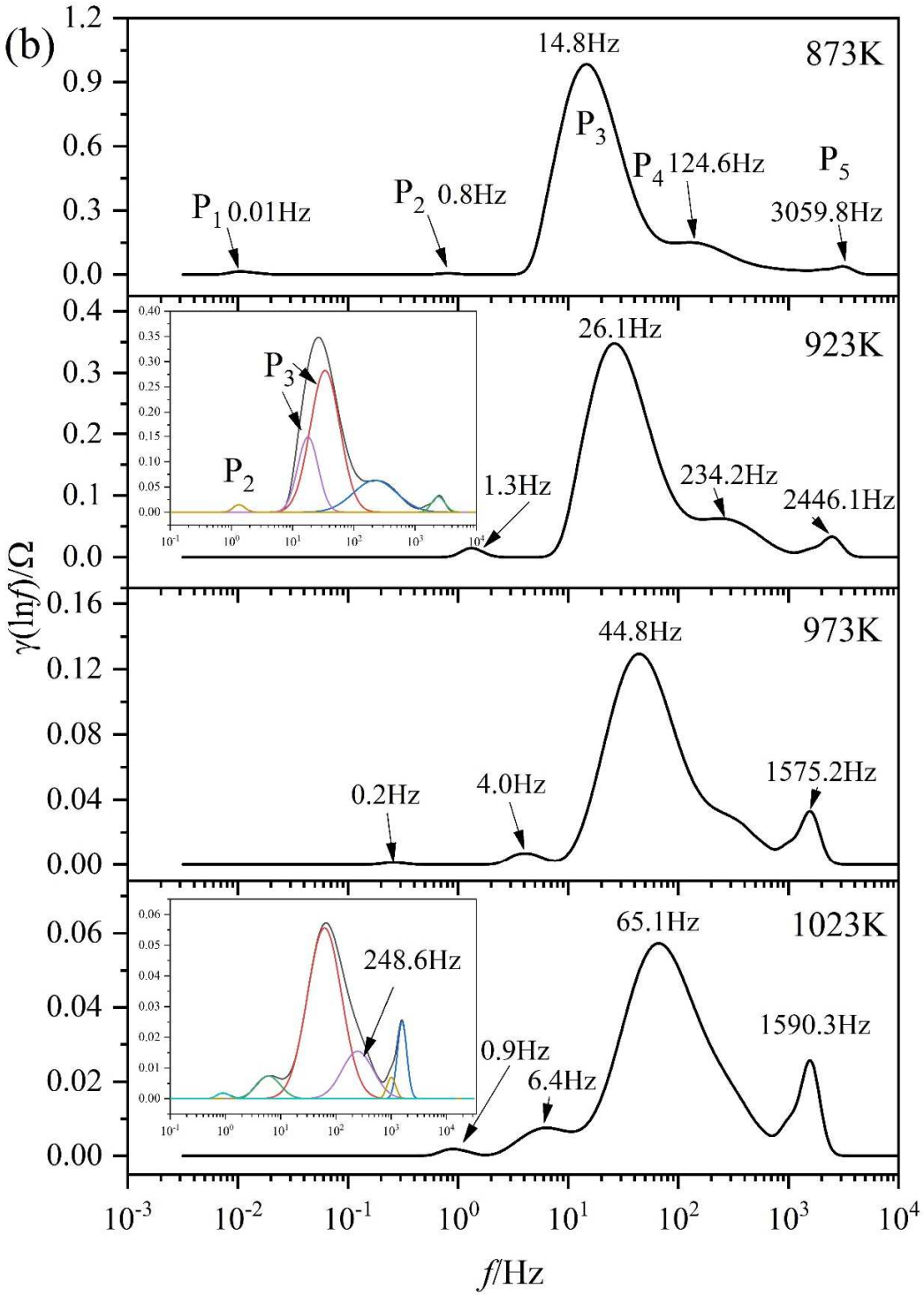
(b)
873K
14.8Hz
P3
P4 124.6Hz
P5
P1 0.01Hz
P2 0.8Hz
3059.8Hz
923K
26.1Hz
P3
P2
1.3Hz
234.2Hz
2446.1Hz
973K
44.8Hz
0.2Hz
4.0Hz
1575.2Hz
1023K
65.1Hz
248.6Hz
0.9Hz
6.4Hz
1590.3Hz
γ(lnf)/Ω
f/Hz

Fig. 6 (B)

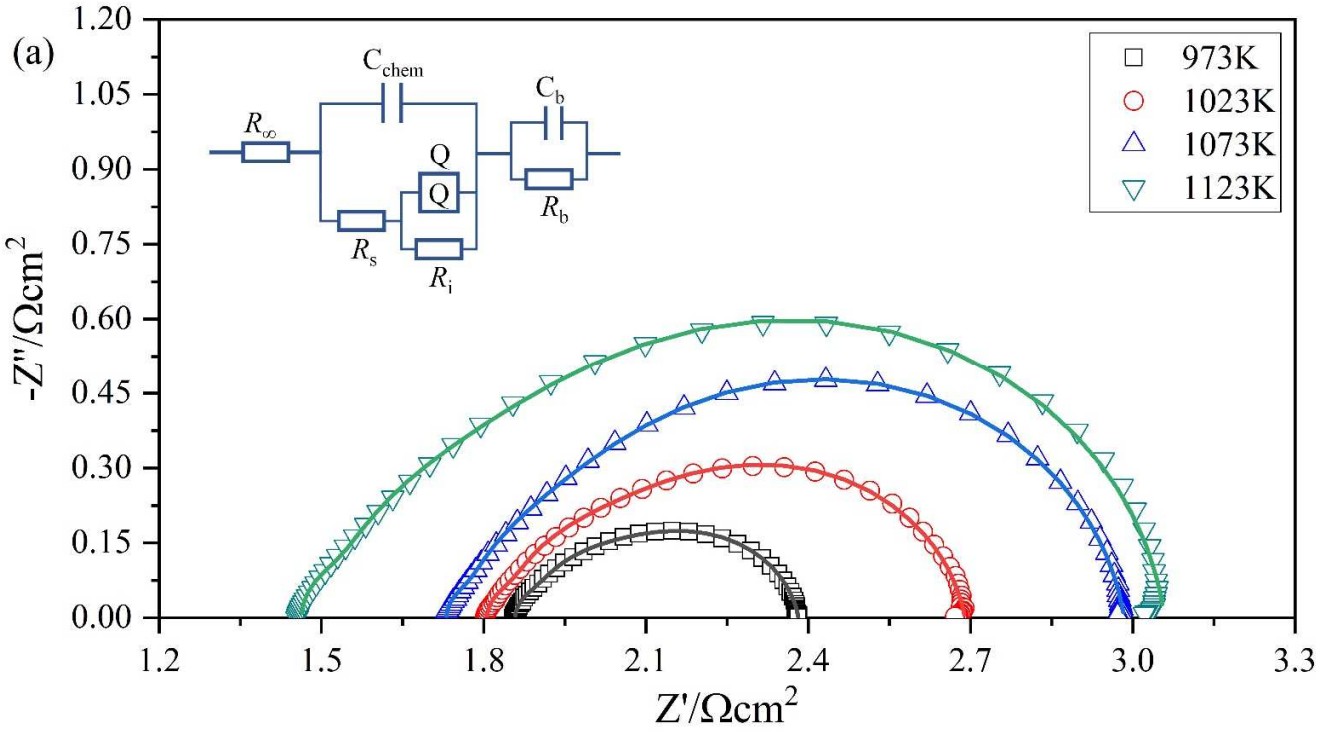
(a)
C_chem
C_b
R_∞
Q
Q
R_s
R_i
R_b
973K
1023K
1073K
1123K
-Z''/Ωcm²
Z'/Ωcm²
1.20
1.05
0.90
0.75
0.60
0.45
0.30
0.15
0.00
1.2
1.5
1.8
2.1
2.4
2.7
3.0
3.3

Fig. 7 (A)

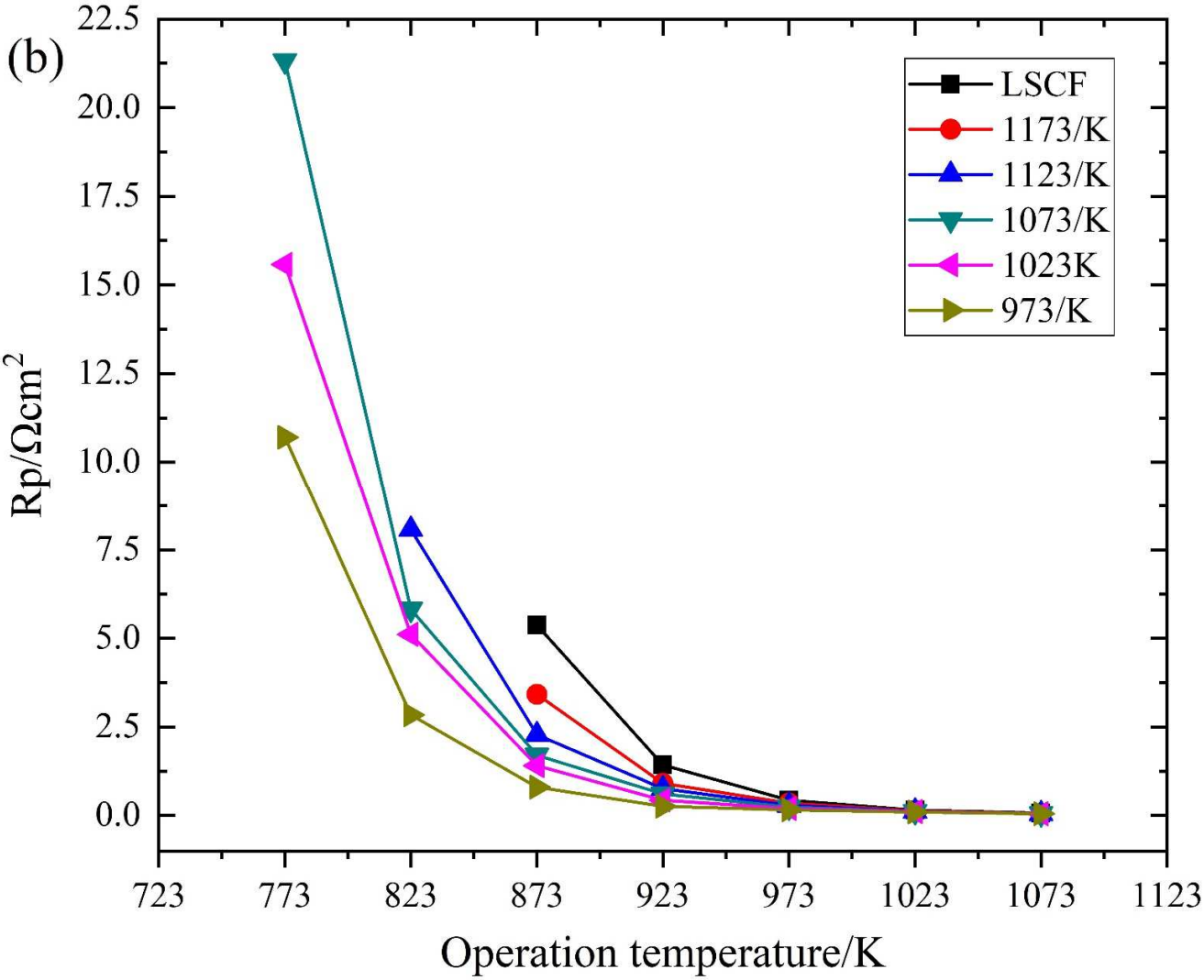
(b)
22.5
20.0
17.5
15.0
12.5
10.0
7.5
5.0
2.5
0.0
Rp/Ωcm2
723
773
823
873
923
973
1023
1073
1123
Operation temperature/K
LSCF
1173/K
1123/K
1073/K
1023K
973/K

Fig. 7 (B)

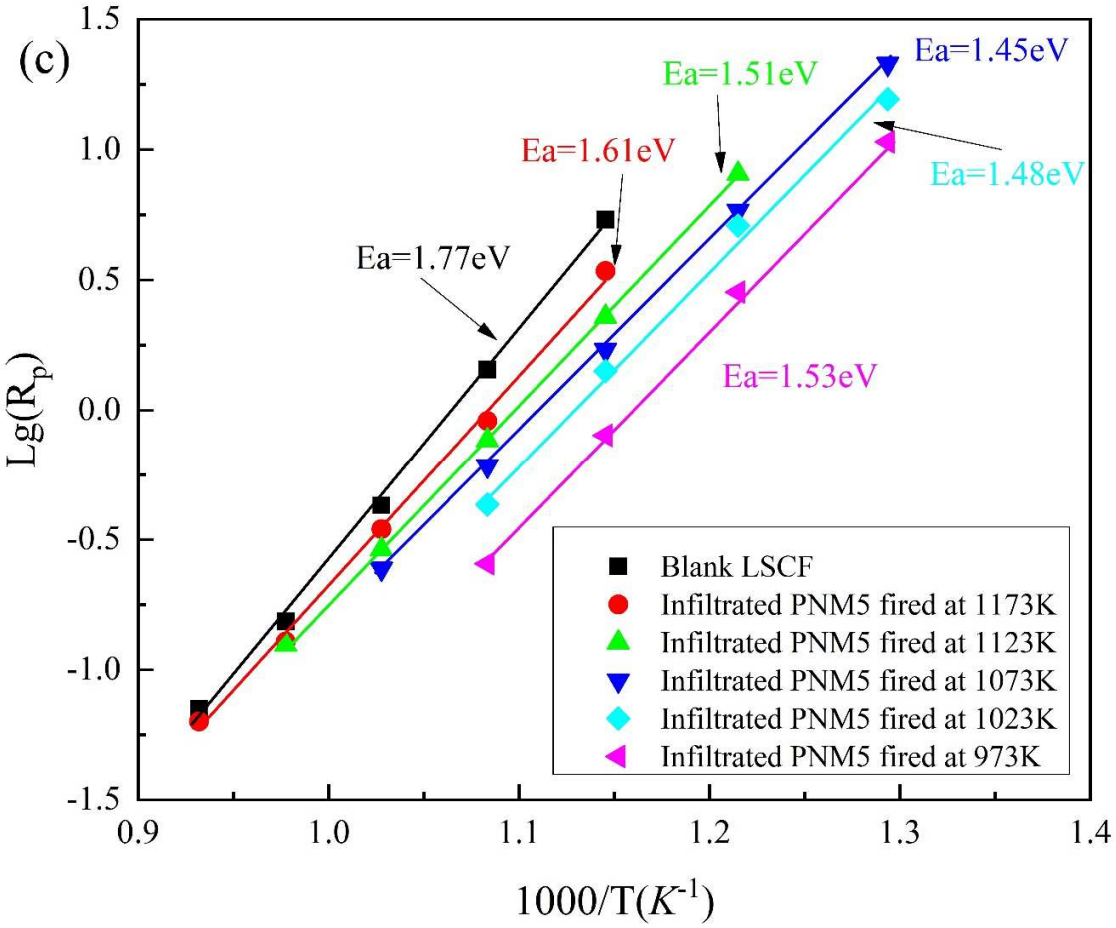
(c)
Ea=1.77eV
Ea=1.61eV
Ea=1.51eV
Ea=1.45eV
Ea=1.48eV
Ea=1.53eV
Blank LSCF
Infiltrated PNM5 fired at 1173K
Infiltrated PNM5 fired at 1123K
Infiltrated PNM5 fired at 1073K
Infiltrated PNM5 fired at 1023K
Infiltrated PNM5 fired at 973K
Lg(R_p)
1000/T(K^-1)
1.5
1.0
0.5
0.0
-0.5
-1.0
-1.5
0.9
1.0
1.1
1.2
1.3
1.4

Fig. 7 (C)

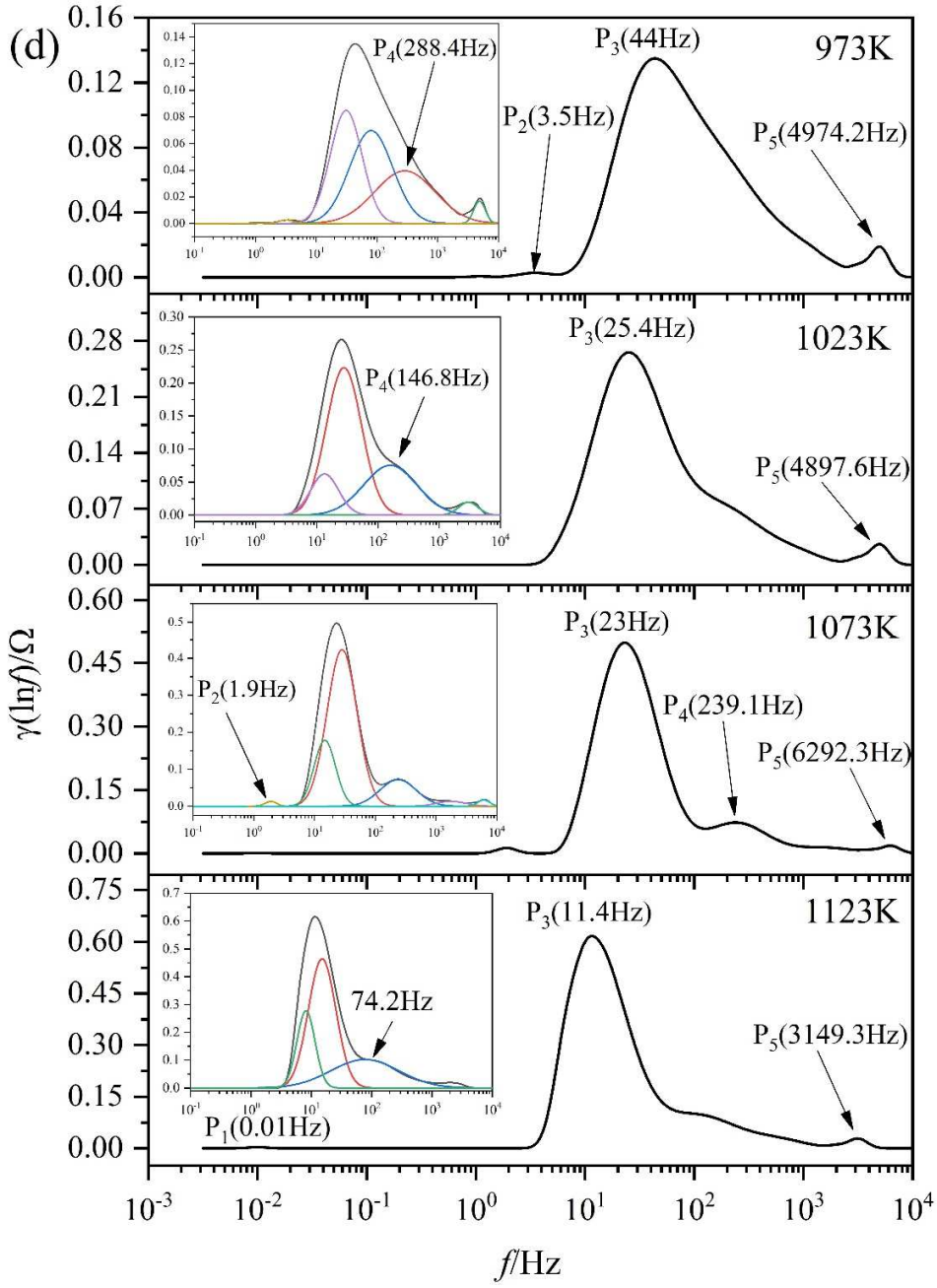
(d)
γ(lnf)/Ω
f/Hz
973K
P3(44Hz)
P2(3.5Hz)
P5(4974.2Hz)
P4(288.4Hz)
1023K
P3(25.4Hz)
P4(146.8Hz)
P5(4897.6Hz)
1073K
P3(23Hz)
P2(1.9Hz)
P4(239.1Hz)
P5(6292.3Hz)
1123K
P3(11.4Hz)
74.2Hz
P5(3149.3Hz)
P1(0.01Hz)

Fig. 7 (D)

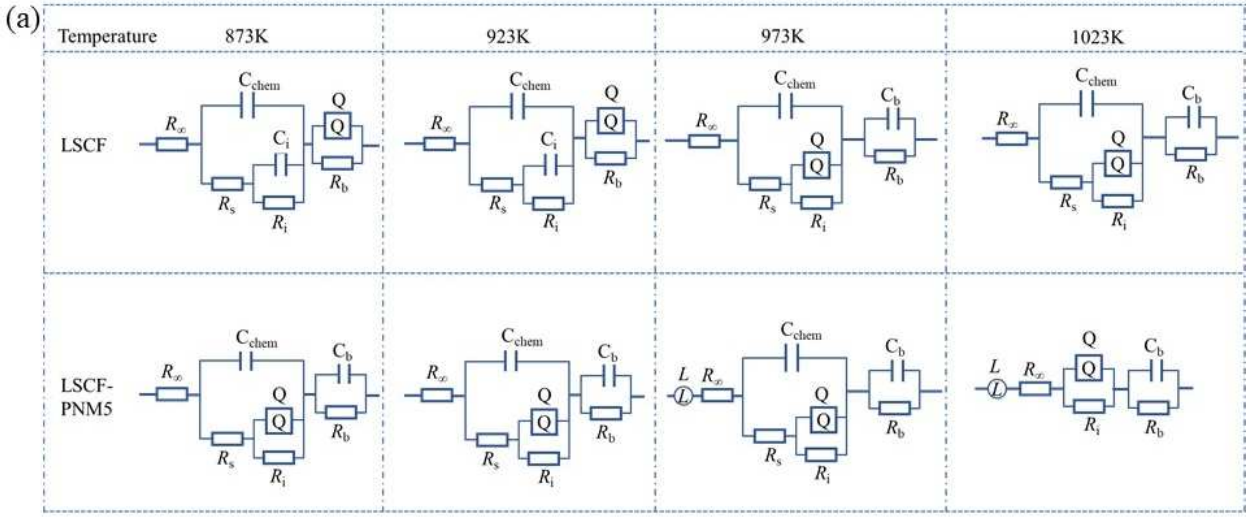
(a)
Temperature
873K
923K
973K
1023K
LSCF
LSCF-
PNM5
C_{chem}
C_b
C_i
Q
R_∞
R_s
R_i
R_b
L

Fig. 8(A)

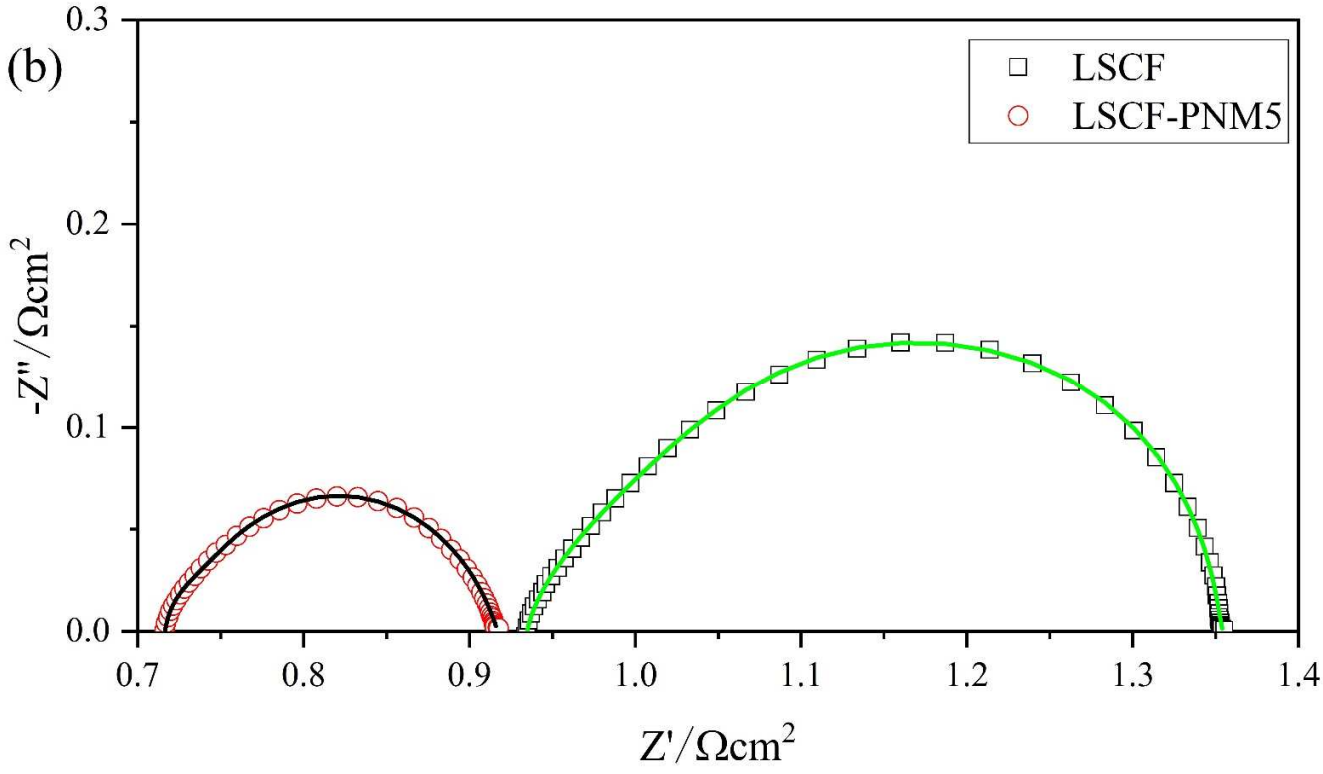
(b)
LSCF
LSCF-PNM5
-Z''/Ωcm^2
Z'/Ωcm^2
0.0
0.1
0.2
0.3
0.7
0.8
0.9
1.0
1.1
1.2
1.3
1.4

Fig. 8(B)

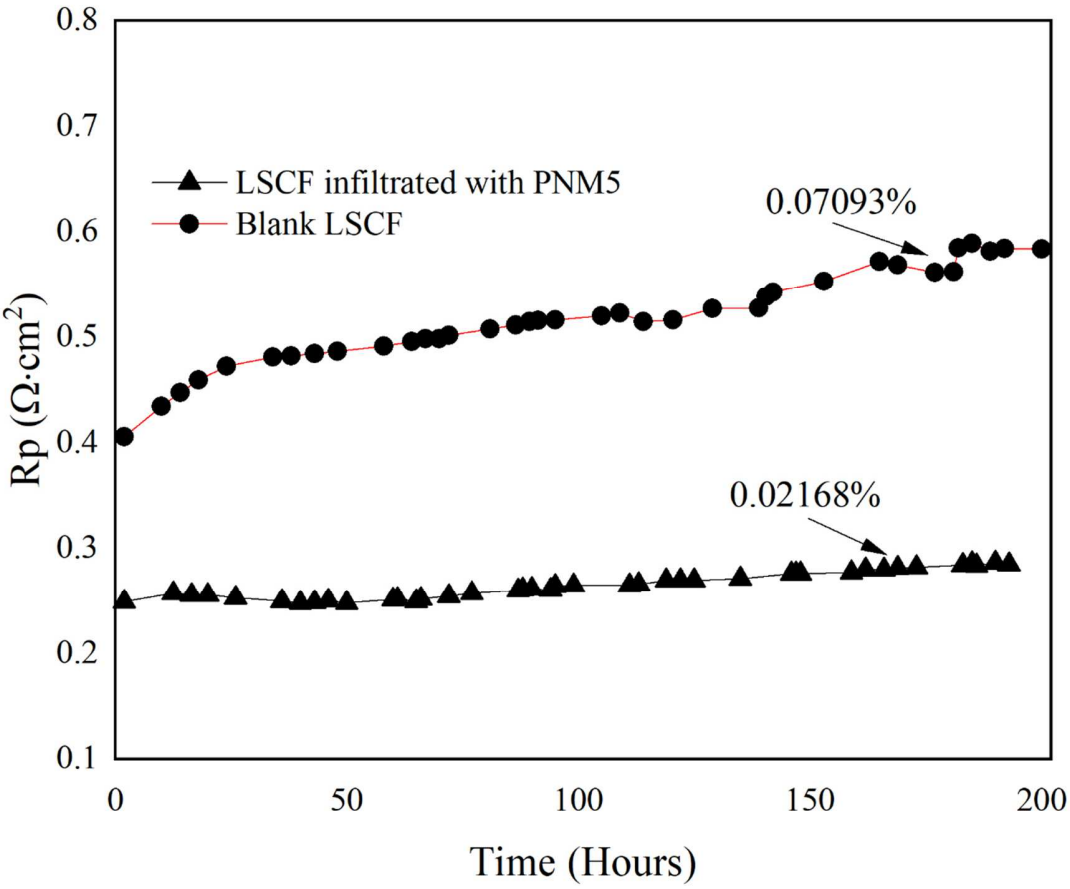
0.8
0.7
0.6
0.5
0.4
0.3
0.2
0.1
Rp (Ω·cm²)
0
50
100
150
200
Time (Hours)
LSCF infiltrated with PNM5
Blank LSCF
0.07093%
0.02168%

Fig. 9

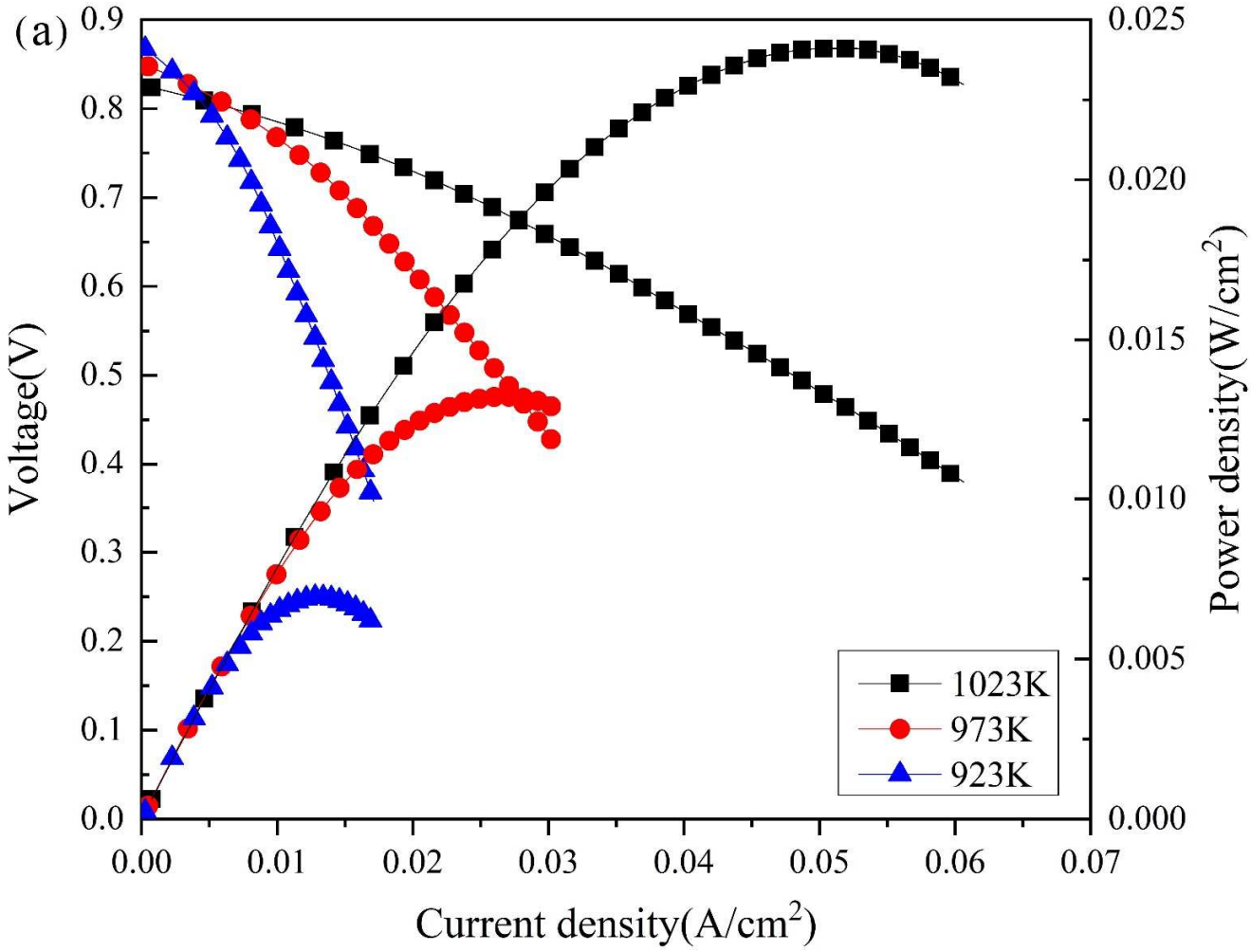
(a)
Voltage(V)
Power density(W/cm^2)
Current density(A/cm^2)
0.0
0.1
0.2
0.3
0.4
0.5
0.6
0.7
0.8
0.9
0.000
0.005
0.010
0.015
0.020
0.025
0.00
0.01
0.02
0.03
0.04
0.05
0.06
0.07
1023K
973K
923K

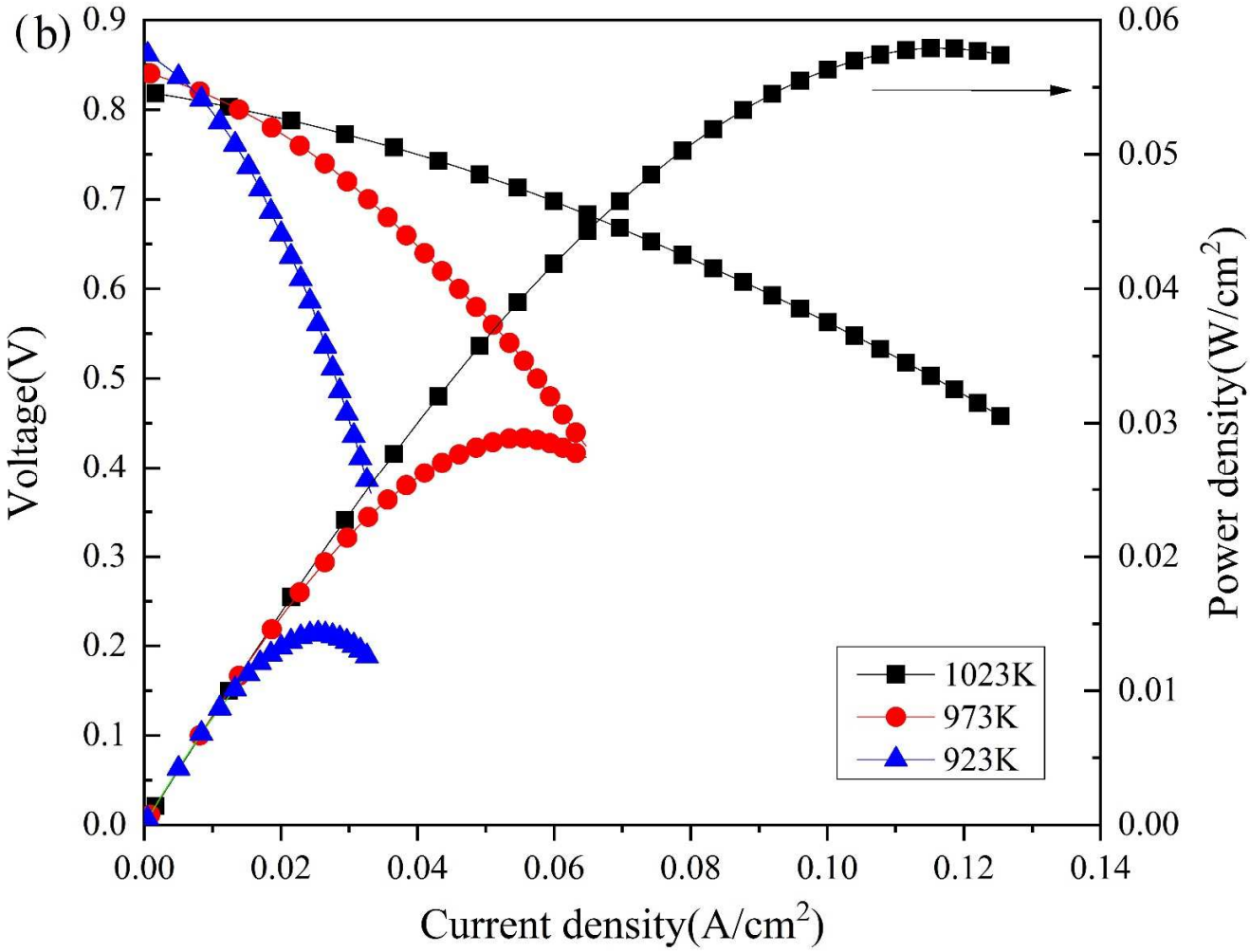
(b)
Voltage(V)
Power density(W/cm^2)
Current density(A/cm^2)
1023K
973K
923K
0.0
0.1
0.2
0.3
0.4
0.5
0.6
0.7
0.8
0.9
0.00
0.01
0.02
0.03
0.04
0.05
0.06
0.00
0.02
0.04
0.06
0.08
0.10
0.12
0.14

Fig. 10